The Astrophysical Journal Supplement Series, 232:15 (28pp), 2017 September https://doi.org/10.3847/1538-4365/aa8667

The DES Bright Arcs Survey: Hundreds of Candidate Strongly Lensed Galaxy Systems from the Dark Energy Survey Science Verification and Year 1 Observations

H. T. Diehl[1], E. J. Buckley-Geer[1], K. A. Lindgren[1], B. Nord[1], H. Gaitsch[1], S. Gaitsch[1], H. Lin[1], S. Allam[1], T. E. Collett[2], C. Furlanetto[3], M. S. S. Gill[4], A. More[5], J. Nightingale[3], C. Odden[1,6], A. Pellico[1], D. L. Tucker[1], L. N. da Costa[7,8], A. Fausti Neto[7], N. Kuropatkin[1], M. Soares-Santos[1], B. Welch[9], Y. Zhang[1], J. A. Frieman[1,9], F. B. Abdalla[10,11], J. Annis[1], A. Benoit-Lévy[10,12,13], E. Bertin[12,13], D. Brooks[10], D. L. Burke[4,14], A. Carnero Rosell[7,8], M. Carrasco Kind[15,16], J. Carretero[17], C. E. Cunha[14], C. B. D'Andrea[18], S. Desai[19], J. P. Dietrich[20,21], A. Drlica-Wagner[1], A. E. Evrard[22,23], D. A. Finley[1], B. Flaugher[1], J. García-Bellido[24], D. W. Gerdes[22,23], D. A. Goldstein[25,26], D. Gruen[4,14], R. A. Gruendl[15,16], J. Gschwend[7,8], G. Gutierrez[1], D. J. James[27,28], K. Kuehn[29], S. Kuhlmann[30], O. Lahav[10], T. S. Li[1], M. Lima[7,31], M. A. G. Maia[7,8], J. L. Marshall[32], F. Menanteau[15,16], R. Miquel[17,33], R. C. Nichol[2], P. Nugent[26], R. L. C. Ogando[7,8], A. A. Plazas[34], K. Reil[4], A. K. Romer[35], M. Sako[18], E. Sanchez[36], B. Santiago[7,37], V. Scarpine[1], R. Schindler[4], M. Schubnell[23], I. Sevilla-Noarbe[36], E. Sheldon[7,38], M. Smith[39], F. Sobreira[7,40], E. Suchyta[41], M. E. C. Swanson[16], G. Tarle[23], D. Thomas[2], and A. R. Walker[28]
(DES Collaboration)

[1] Fermi National Accelerator Laboratory, P.O. Box 500, Batavia, IL 60510, USA; diehl@fnal.gov
[2] Institute of Cosmology & Gravitation, University of Portsmouth, Portsmouth, PO1 3FX, UK
[3] University of Nottingham, School of Physics and Astronomy, Nottingham NG7 2RD, UK
[4] SLAC National Accelerator Laboratory, Menlo Park, CA 94025, USA
[5] Kavli IPMU (WPI), UTIAS, The University of Tokyo, Kashiwa, Chiba 277-8583, Japan
[6] Phillips Academy, Andover, MA 01810, USA
[7] Laboratório Interinstitucional de e-Astronomia—LIneA, Rua Gal. José Cristino 77, Rio de Janeiro, RJ—20921-400, Brazil
[8] Observatório Nacional, Rua Gal. José Cristino 77, Rio de Janeiro, RJ—20921-400, Brazil
[9] Department of Astronomy and Astrophysics, University of Chicago, 5640 South Ellis Avenue, Chicago, IL 60637, USA
[10] Department of Physics & Astronomy, University College London, Gower Street, London, WC1E 6BT, UK
[11] Department of Physics and Electronics, Rhodes University, P.O. Box 94, Grahamstown, 6140, South Africa
[12] CNRS, UMR 7095, Institut d'Astrophysique de Paris, F-75014, Paris, France
[13] Sorbonne Universités, UPMC Univ Paris 06, UMR 7095, Institut d'Astrophysique de Paris, F-75014, Paris, France
[14] Kavli Institute for Particle Astrophysics & Cosmology, P.O. Box 2450, Stanford University, Stanford, CA 94305, USA
[15] Department of Astronomy, University of Illinois, 1002 W. Green Street, Urbana, IL 61801, USA
[16] National Center for Supercomputing Applications, 1205 West Clark Street, Urbana, IL 61801, USA
[17] Institut de Física d'Altes Energies (IFAE), The Barcelona Institute of Science and Technology, Campus UAB, E-08193 Bellaterra (Barcelona) Spain
[18] Department of Physics and Astronomy, University of Pennsylvania, Philadelphia, PA 19104, USA
[19] Department of Physics, IIT Hyderabad, Kandi, Telangana 502285, India
[20] Excellence Cluster Universe, Boltzmannstr. 2, D-85748 Garching, Germany
[21] Faculty of Physics, Ludwig-Maximilians-Universität, Scheinerstr. 1, D-81679 Munich, Germany
[22] Department of Astronomy, University of Michigan, Ann Arbor, MI 48109, USA
[23] Department of Physics, University of Michigan, Ann Arbor, MI 48109, USA
[24] Instituto de Fisica Teorica UAM/CSIC, Universidad Autonoma de Madrid, E-28049 Madrid, Spain
[25] Department of Astronomy, University of California, Berkeley, 501 Campbell Hall, Berkeley, CA 94720, USA
[26] Lawrence Berkeley National Laboratory, 1 Cyclotron Road, Berkeley, CA 94720, USA
[27] Astronomy Department, University of Washington, Box 351580, Seattle, WA 98195, USA
[28] Cerro Tololo Inter-American Observatory, National Optical Astronomy Observatory, Casilla 603, La Serena, Chile
[29] Australian Astronomical Observatory, North Ryde, NSW 2113, Australia
[30] Argonne National Laboratory, 9700 South Cass Avenue, Lemont, IL 60439, USA
[31] Departamento de Física Matemática, Instituto de Física, Universidade de São Paulo, CP 66318, CEP 05314-970, São Paolo, SP, Brazil
[32] George P. and Cynthia Woods Mitchell Institute for Fundamental Physics and Astronomy, and Department of Physics and Astronomy, Texas A&M University, College Station, TX 77843, USA
[33] Institució Catalana de Recerca i Estudis Avançats, E-08010 Barcelona, Spain
[34] Jet Propulsion Laboratory, California Institute of Technology, 4800 Oak Grove Drive, Pasadena, CA 91109, USA
[35] Department of Physics and Astronomy, Pevensey Building, University of Sussex, Brighton, BN1 9QH, UK
[36] Centro de Investigaciones Energéticas, Medioambientales y Tecnológicas (CIEMAT), Madrid, Spain
[37] Instituto de Física, UFRGS, Caixa Postal 15051, Porto Alegre, RS—91501-970, Brazil
[38] Brookhaven National Laboratory, Bldg 510, Upton, NY 11973, USA
[39] School of Physics and Astronomy, University of Southampton, Southampton, SO17 1BJ, UK
[40] Instituto de Física Gleb Wataghin, Universidade Estadual de Campinas, 13083-859, Campinas, SP, Brazil
[41] Computer Science and Mathematics Division, Oak Ridge National Laboratory, Oak Ridge, TN 37831, USA
Received 2017 May 3; revised 2017 July 18; accepted 2017 August 7; published 2017 September 22

Abstract

We report the results of searches for strong gravitational lens systems in the Dark Energy Survey (DES) Science Verification and Year 1 observations. The Science Verification data span approximately 250 sq. deg. with a median *i*-band limiting magnitude for extended objects (10σ) of 23.0. The Year 1 data span approximately 2000 sq. deg. and have an *i*-band limiting magnitude for extended objects (10σ) of 22.9. As these data sets are both wide and deep, they are particularly useful for identifying strong gravitational lens candidates. Potential strong gravitational lens candidate systems were initially identified based on a color and magnitude selection in the DES

object catalogs or because the system is at the location of a previously identified galaxy cluster. Cutout images of potential candidates were then visually scanned using an object viewer and numerically ranked according to whether or not we judged them to be likely strong gravitational lens systems. Having scanned nearly 400,000 cutouts, we present 374 candidate strong lens systems, of which 348 are identified for the first time. We provide the R.A. and decl., the magnitudes and photometric properties of the lens and source objects, and the distance (radius) of the source(s) from the lens center for each system.

Key words: galaxies: high-redshift – gravitational lensing: strong

Supporting material: machine-readable tables

1. Introduction

Gravitational lensing occurs because the trajectory of photons from a distant object is deflected while passing through the gravitational field of a less-distant massive object along the line of sight with the observer. We call the more distant object a "source" and the less-distant object a "lens." If the source, the lens, and the observer are sufficiently separated and collinear, and if the mass of the lens is sufficiently large, then the apparent shape of the source can be noticeably distorted. Indeed, the source can appear as an extended arc or ring or even appear multiple times around the lens. This effect is called "strong" gravitational lensing.

Strong gravitational lens systems provide opportunities to study both astrophysics and cosmology. These systems provide an opening for studying properties of distant galaxies. Because the surface brightness of a source is unchanged during lensing, magnification of the source provides amplification of the image flux and allows studies of details that would otherwise be unresolved or too faint for ground-based investigation (e.g., Kostrzewa-Rutkowska et al. 2014). Sources with relatively large redshift are used for studies of star formation and metallicity in young galaxies (e.g., Bayliss et al. 2014). Studies of the lens systems, whether galaxies, groups, or clusters, provide information on their mass distribution, including the dark matter (Koopmans et al. 2009; Wiesner et al. 2012; Treu & Ellis 2014; Newman et al. 2015). Special cases of strong lens systems can be used to study cosmology. For instance, for lensed time-varying sources such as galaxies that contain quasars, the different appearances of the source may have differing times-of-flight and this information can be used (Refsdal 1964; Blandford & Narayan 1992) to extract the expansion history between source, lens, and observer (Schechter et al. 1997; Suyu et al. 2013, 2017; Birrer et al. 2016; Bonvin et al. 2017). Lens systems with multiple sources at differing redshifts can provide (Link & Pierce 1998; Gavazzi et al. 2008; Jullo et al. 2010; Collett & Auger 2014) complementary information (Collett et al. 2012) about the expansion history, independent of the Hubble constant.

While individual strong lens (SL) systems provide details of the characteristics of the lens and source objects, studies of statistically large samples of strong lensing systems have been considered as probes of the growth of structure and cosmology (-Meneghetti et al. 2013). Realistic simulations (Li et al. 2016) of SL systems make it possible to compare (Xu et al. 2016) large samples with theoretical expectations. While the computations can easily generate O(10,000) or more simulated strong lensing systems, samples of more than a few dozen actual strong lens candidates from a single survey are scarce.

A number of automated methods for identifying strong lens candidates have been developed. These include a search for elongated objects (Alard 2006), an ARCFINDER (Seidel & Bartelmann 2007) that identifies SL candidates associated with galaxy clusters or groups, analysis of third-order moments of galaxy shapes (Kubo & Dell'Antonio 2008) to find systems with arcs in the Deep Lens Survey (Wittman et al. 2006), principal component analysis (PCA) to identify (Joseph et al. 2014; Paraficz et al. 2016) SL systems with complete or nearly complete Einstein rings, and Deep Learning (Lanusse et al. 2017) and neural network (de Bom et al. 2017; Petrillo et al. 2017) analysis of galaxy shapes. Another new method, YATTALENS (Sonnenfeld et al. 2017), identifies galaxy–galaxy lens candidates with arc-like features by modeling the source and lens galaxies and subtracting the lens galaxy from the image. Attaining large samples of real lenses with a variety of morphologies is important for vetting and testing the automated lens-finding algorithms, particularly for identification of group and cluster-scale SL systems. While these automated techniques show promise and could improve the statistical analysis of SL systems, traditionally productive searches have required labor-intensive techniques including visual scanning of candidate systems.

Wide-field surveys present a rich data sample in which to look for strong lens systems. The 1.64 deg^2 *Hubble Space Telescope* COSMOS survey field yielded 67 galaxy–galaxy lens candidates (Faure et al. 2008). The SDSS data yielded 19 confirmed systems to the Sloan Bright Arcs Survey (Allam et al. 2007; Diehl et al. 2009; Kubo et al. 2009, 2010; Lin et al. 2009), more than 30 confirmed and 50 additional candidate lenses to the CASSOWARY survey (Belokurov et al. 2009; Pettini et al. 2010; Stark et al. 2013), and 68 new galaxy clusters with giant arcs (Wen et al. 2011). The CFHTLS-Strong Lensing Legacy Survey (More et al. 2012) sample includes 54 systems with promising lenses, including 12 giant arcs, found in 150 deg^2 using the ARCFINDER method. The Blanco Cosmology Survey yielded one serendipitous discovery (Buckley-Geer et al. 2011). Gavazzi et al. (2014) provides 49 confirmed strong lens systems identified using RINGFINDER on CFHTLS data. Crowdsourcing (Marshall et al. 2016) has led to discovery of 29 promising and 59 total (More et al. 2016) new strong lens systems in the CFHTLS data. Three different methods, including YATTALENS, were used to search the Hyper Suprime-Cam Subaru Strategic Program (HSC SSP) images. The program (Sonnenfeld et al. 2017) yielded 333 candidates from an area of 442 deg^2. The HSC SSP sample is comparable in size and complementary to the result of this paper, as their candidates are principally galaxy–galaxy lenses with a small Einstein radius. Previous searches of the Dark Energy Survey data initially yielded six confirmed strongly lensed galaxies (Nord et al. 2016) in the early DES data, and more recently yielded eight more (B. Nord et al. 2017, in preparation), and four gravitationally lensed quasars (Agnello et al. 2015; Lin et al. 2017; Ostrovski et al. 2017). Other SL systems discovered using the DECam imager include the Canarias Einstein Ring (Bettinelli et al. 2016).

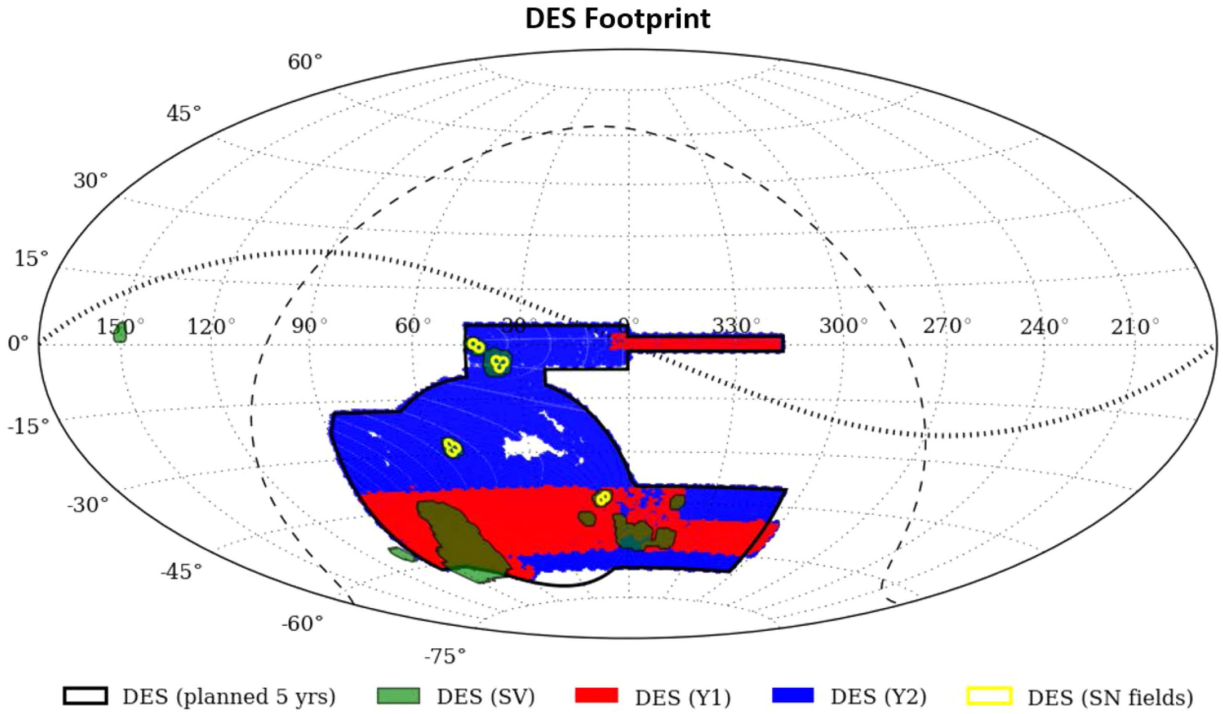

Figure 1. The Dark Energy Survey observational footprint. This result is based on searches of the SV (green) and Y1 (red and yellow) fields. We note that some of the area of Y1 overlaps with the SV fields.

Searches of massive galaxy clusters have yielded many strong lenses. A search (Hennawi et al. 2008) of 240 massive galaxy clusters yielded 16 strong lens systems with $>10''$ radius and 21 additional SL candidates, where the lensing interpretation is based on the morphology of the systems. The South Pole Telescope identified (Reichardt et al. 2013) massive clusters using the Sunyaev–Zel'dovich effect (inverse Compton scattering of the cosmic microwave background radiation off hot electrons in the intergalactic medium within the cluster) (Sunyaev & Zel'dovich 1972) in a 2500 sq. deg. field that overlaps the same field that is presented in this paper. Many of the clusters have strong lens systems apparent in optical imaging follow-up observations (Staniszewski et al. 2009; Song et al. 2012; Aravena et al. 2013; Bleem et al. 2015). These are all compiled in one paper (Bleem et al. 2015). One of these was previously reported and studied in Buckley-Geer et al. (2011). Others were also found and reported (Menanteau et al. 2010a, 2012) in the ACT survey data.

The MASTER LENS DATABASE (L. Moustakas & J. Brownstein 2017, in preparation) lists[42] 657 strong lens candidates, in three grades, to date. Ongoing and upcoming surveys will discover many more. Predictions for the number of lenses depend on the depth and area of the survey and range from a few thousand for the full Dark Energy Survey to more than a hundred thousand for near-future surveys (Oguri & Marshall 2010; Collett 2015).

In this paper we report the discovery of 348 previously unreported (and 26 additional) strong gravitational lens candidates from the Dark Energy "Science Verification" and "Year 1" data. This paper is organized as follows. In Section 2 we describe the Dark Energy Survey Science Verification and Year 1 observations and catalogs. In Section 3 we describe our strong gravitational lens search procedures. In Section 4 we describe the results from the searches and provide the properties of the candidate lens systems. We highlight some of the systems that have notable properties. Finally, in Section 5 we recapitulate the results and provide prospects for the analysis of the full DES wide-field.

2. Dark Energy Survey Imaging Data

The Dark Energy Survey is in the midst of imaging 5000 sq. deg. of the southern galactic cap using the Dark Energy Camera (DECam) (Flaugher et al. 2015), which is operated on the 4 m Victor M. Blanco Telescope at Cerro Tololo Interamerican Observatory (CTIO) near La Serena, Chile.

DECam installation was completed in 2012. There followed a period of commissioning the new instrument and recommissioning the telescope. Science verification (SV) spanned 79 nights or half-nights from 2012 November 1, to 2013 February 22. The main SV wide-field (WF) survey areas amounted to ~250 sq. deg. at non-uniform depth and data quality. The median i-band limiting magnitude for extended[43] objects (10σ) was 23.0. In a subset of the area, amounting to about 150 sq. degs., the survey is more than a half magnitude deeper and comparable to what we expect in the final 5-year long survey (The Dark Energy Survey Collaboration 2016). This was accomplished by observing each part of those fields 10 times in each of the 5 filters: the g, r, i, z, and Y-bands. The exposure times varied with fields and were usually of 90 s duration, with most Y-band exposures taken with 45 s duration. The DES observing footprint, including the location of the SV fields, is described in The Dark Energy Survey Collaboration (2016) and is shown in Figure 1.

The first full observing season, Year 1 (Y1), spanned 119 nights or half-nights from 2013 August 31 to 2014 February 9.

[42] http://admin.masterlens.org/index.php

[43] https://des.ncsa.illinois.edu/releases/sva1/doc

The Y1 wide-field (WF) survey observations were concentrated in two areas: one of about 150 sq. deg. near the celestial equator that included a part of SDSS Stripe 82 (Annis et al. 2014), and a much larger region of roughly 1800 sq. deg. from -60° to -40° decl. that overlapped the area mapped in microwaves by the South Pole Telescope (Carlstrom et al. 2011). Generally, we observed those fields four times in each of the five filters: the g, r, i, z, and Y-bands. The exposures were of 90 s duration for the g through z bands and 45 s for the Y-band. The average FWHM of the point-spread function (PSF) for Y1 wide-survey exposures in the r, i, z bands was 0.94 arcsec, while the FWHM for the g, Y-bands was 1.17 arcsec. The i-band limiting magnitude for extended objects (10σ) was 22.9 (Drlica-Wagner et al. 2017). In addition to the wide-field survey, DES performed a time-domain ("supernova") survey during the same time period, visiting 10 fields in the g, r, i, and z-band filters with an approximately weekly cadence and at much greater depth (Kessler et al. 2015) than the wide-field survey. More details of the operations, data collection procedures, and observing results are available (Diehl et al. 2014). Figure 1 also shows the DES Y1 and SN fields.

The data were processed by the Dark Energy Survey Data Management (DESDM) system (Mohr et al. 2012; R. Gruendl et al. 2017, in preparation) in three pipelined stages: single-epoch "detrending," photometric calibration, and coaddition. The detrending operation removes the instrumental signature from the individual exposures. This includes corrections for cross-talk between amplifiers on the CCDs, subtraction of the bias, removal of the overscan and masking of "bad" pixels, application of a flat-field frame, an illumination correction determined on a CCD by CCD basis, a correction for the pupil ghost, a sky-background subtraction, and an artifact (cosmic ray) removal. Single-epoch catalogs were produced using PSFEx (Bertin 2011) and SExtractor (Bertin & Arnouts 1996). Astrometric calibration is performed by matching bright stars on each exposure to reference stellar catalogs using SCAMP (Bertin 2006). Next, a photometric calibration is made. The "Global Calibration Module" starts with a list of exposures taken under photometric conditions (i.e., no extinction due to clouds or atmospheric dust), determines the magnitudes of many stars in each filter, and propagates that information across the many non-photometric overlapping exposures to determine a zero-point for each CCD in each exposure. Relative photometry of better than 2% rms accuracy was achieved. The relative photometric calibration was tied to an AB absolute system through targeted observations of bright spectrophotometric standards, again at about the 1%–2% level. Finally, the exposures in each filter were coadded using SWarp (Bertin et al. 2002) in 10,000 by 10,000 pixel "tiles" $0.^\circ72$ on a side. SExtractor was then rerun on these coadded tiles to form catalogs of objects. A weighted combination of the coadded $r+i+z$ "detection" tiles was used for identifying objects. The separation or "deblending" of closely positioned (or even overlapping) objects is a challenge, where the goal is to balance completeness against the spurious separation of features within a single galaxy. The deblending was performed using the detection images. The standard SExtractor 2.0 algorithm, which we used for the deblending, is not optimized for closely spaced lenses and sources or those in dense galaxy cluster cores (Zhang et al. 2014). The object catalogs contain the list of objects, their shapes, and their astrometric and photometric properties calculated from the coadd tile for each filter. Model magnitudes are fit to galaxies using a PSF derived from each coadd tile. Unless noted otherwise, the SExtractor MAG_AUTO magnitudes are the primary measures of coadd flux used in further analysis. There were typically 25,000 to 40,000 objects in the catalog of a full area tile.

The 580 sub-catalogs from SV are called "SVA1," where the A1 stands for "Annual Release #1." The 3778 sub-catalogs from Y1 are called "Y1A1." In both SVA1 and Y1A1 many of the sub-catalogs are made from incompletely observed tiles; these are typically from along the boundaries of the fields. The SVA1 catalog[44] contains 46M objects. The Y1A1 catalog contains 140M objects. Additional details about the Y1A1 WF processing and catalog can be found in Drlica-Wagner et al. (2017).

3. Gravitational Lens Candidate Search Procedures

We applied several different techniques, described below, to search for SL systems using the SVA1 and Y1A1 data. The different techniques have some common elements. For each technique we created a list of potential lens systems. These lists were loaded onto the "DES Science Portal," a tool for visualizing the DES fields that can also provide catalog information about the objects. We used the Portal to produce small, 3-color (g, r, and i-band) cutout images, typically $55'' \times 55''$, centered on each of the systems. Several people, either scientists with experience identifying SL systems or students trained to do so, scanned pages of cutouts. At least two people scanned every cutout among the lists. Each page required 30 to 60 s to scan, depending on the speed of the scanner. Figure 2 shows a sample page of candidates as seen on the Portal. Potential SL candidates were identified by the occurrence of an apparent arc, or a pattern of arc-like knots or objects suggestive of an instance of strong lensing. It was not required that the potential sources or lenses that we identified were part of the selection that caused the cutout to be made in the first place. Interesting candidates were flagged for further evaluation. Some bright or particularly interesting candidates were immediately designated for further study. This initial process occurred over a period of about a year and a half.

Each search uncovered unique, new systems, as well as some that eventually became very familiar, these having been "discovered" multiple times. Eventually, as further effort would lead to diminishing returns—mostly in the form of fainter systems, we stopped creating new searches. After we decided to terminate further searches, short lists of systems identified as candidates were compiled and all re-ranked, over a period of a few days, by a team of five scientists. Each person assigned a score of 0 to 2 to each system—0 points if the system was thought to not be a SL candidate, 1 point if it might be, and 2 points if the system was expected to be an instance of strong lensing. The maximum summed score that a system could attain was a 10. Systems with a total score of at least 3 were taken as the final list for this paper. The candidate rankings of 3 to 10 span the range from "possible" to "probable" to "definite" SL systems, with rankings consistent with those used in the Master Lens Database (L. Moustakas & J. Brownstein 2017, in preparation) and other graded samples of similar SL candidates.

[44] https://des.ncsa.illinois.edu/releases/sva1/doc

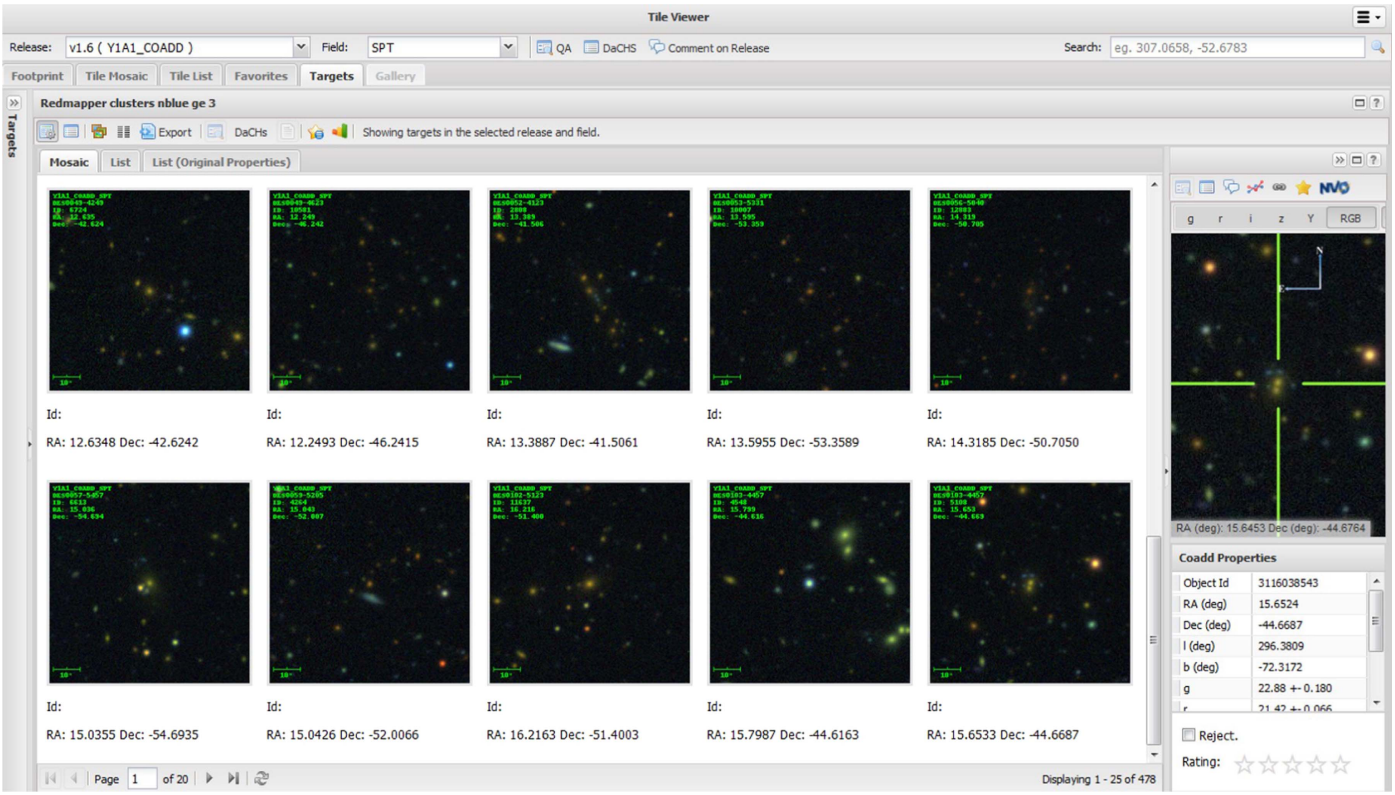

Figure 2. Typical page of cutouts as viewed on the Science Portal. The cutouts are 55″ on a side. The Portal displayed 25 cutouts on each page. These were viewed on a computer screen large enough to visualize the details in each system.

We did not apply our search techniques to any samples of simulated strong lenses.

In this section we describe the four separate search procedures and the number of candidates that each produced.

3.1. A Search around Galaxy Clusters Identified by the South Pole Telescope

Because galaxy clusters are among the most massive structures in the Universe, they are with relatively high-probability candidates for gravitational lenses. The South Pole Telescope (SPT) used the Sunyaev–Zel'dovich effect to identify massive galaxy clusters in a 2500 sq. deg. field that is substantially overlapped by the Y1 data. The complete SPT catalog comprises 677 galaxy clusters (Bleem et al. 2015), with a signal-to-noise threshold of 4.5. Our "first pass" search of the Y1A1 catalogs around the position of these galaxy clusters yielded 66 SL candidates; 34 of these were given a rank of three or more in the final evaluation. The mean rank for those 34 was 6.9 (out of 10).

The SPT Collaboration followed up some of the 677 galaxy clusters with *Hubble Space Telescope* or deep *Magellan*/Megacam imaging and identified (Bleem et al. 2015) 48 of those as being gravitational lenses. We comment, in Section 4, on the overlap between the SPT lens sample and those that we identified.

3.2. "Blue Near Anything Knot" Searches

We searched the SV and Y1 catalogs for SL candidates using a "Blue Near Anything" (BNA) algorithm, originally motivated in Kubik (2007). This algorithm aimed at identifying strong lensing of star-forming Lyman break galaxies and Lyα-emitting galaxies lensed by massive luminous red galaxies (LRGS).

We developed the BNA algorithm using the SV catalogs. The procedure was performed on a single coadd tile at a time and is illustrated in Figure 3. First a list of candidate lens galaxies is created. The criteria for a galaxy to be in the list of possible lenses are that at least one of the *r*-band, *i*-band, or *z*-band magnitudes is less than 21. Selection criteria on SExtractor outputs removed galaxies that were faint, objects that were not well deblended, objects that are likely to be stars, and artifacts left over from objects with saturated pixels. There were typically 4000 to 5000 candidate lens galaxies per tile. Next we formed a list of source candidates. The criteria for an object to be in the list of possible sources are that at least one of the the magnitudes for the *g*-band, *r*-band, or *i*-band must be less than 21, and that the object is not poorly deblended or contains saturated pixels. We did not make a star-galaxy separation because we wanted to preserve the possibility of identifying strongly lensed quasars for which the appearance of the knots are star-like (Reed et al. 2015). A color selection was applied to select blue source candidates; we required that $g - r < 1.0$ and that $r - i < 1.0$. There were typically 2000 to 3000 candidate source objects per tile. Next, for each object in the lens list we identified the objects in the source list that were within 8″ of the lens. Then we identified the largest set of those sources, associated with a given lens candidate object, that each had a similar color, where the "similar" requirement was that $|\Delta(g - r)|$ and $|\Delta(r - i)|$ both be less than 0.25 magnitudes. This corresponds to about three times the uncertainty in the color of a given source object at the faintest allowed magnitude. Although we do not impose color cuts on the lens selection, this algorithm predominantly finds blue-colored

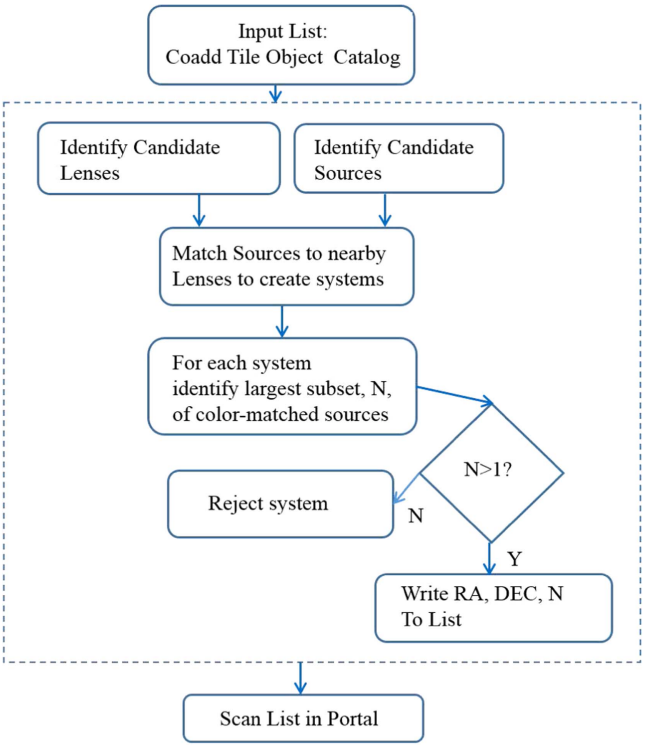

Figure 3. Typical flowchart for the "Blue Near Anything" and "Red Near Anything" search algorithms. The box with the dotted outline is a single computer program. The redMaGiC search flowchart would be similar to this one but with the "Input List" changed to "redMaGiC Galaxies" and the step where we identify the best set of source candidates for a given lens candidate omitted.

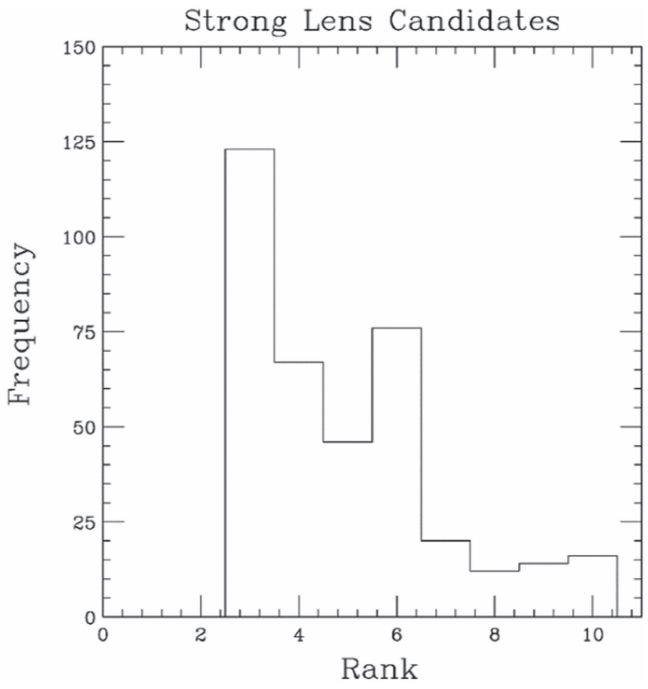

Figure 4. Ranks of the 374 systems for which the rank was 3 or more. The mean (median) rank of these systems was 4.9 (4).

source galaxies lensed by red galaxies and galaxy clusters. For visual scanning, we kept any system that had two or more matched source objects. We refer to this as the BNA 2+

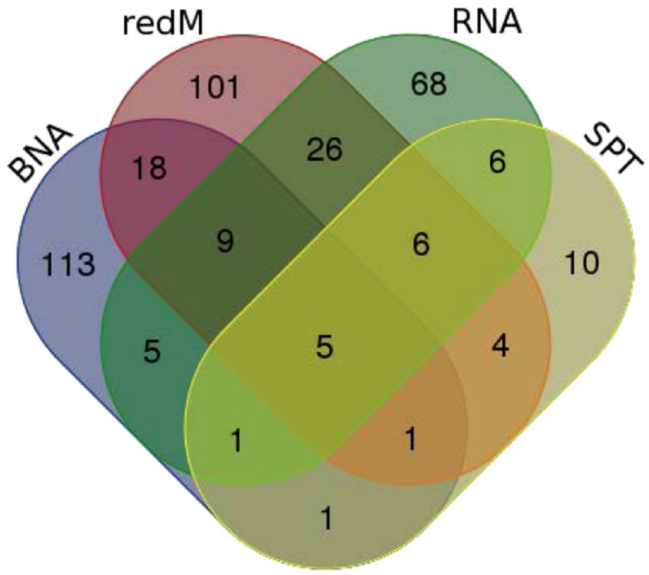

Figure 5. Distribution of rank >3 systems according to the various search algorithms that identified the candidate system. The "One Knot" search results are combined with the other "Blue Near Anything" searches. While each search produced many systems that were not identified by the others, the BNA search had the highest fraction, 74%, of uniquely identified systems.

Table 1
Summary of the Number of Objects Visually Scanned, the Number Ranked, and the Count of Those with Ranks > 3 for the Various Searches

Search	Data Source	# Scanned	# Ranked	Rank > 3
SPT Clusters	Y1	677	66	34
BNA 2+	SV	14820	⋯	⋯
BNA 2+	Y1	75557	⋯	⋯
BNA 2+	subtotal	90377	211	96
BNA 1K	SV	18010	14	⋯
BNA 1K	Y1	132725	107	⋯
BNA 1K	subtotal	150735	121	75
BNA	Combined	241112	292	153
RedM	Y1	13854	374	170
RNA SV 3+	SV	3091	⋯	⋯
RNA Y1 2+	Y1	129283	⋯	⋯
RNA	Combined	132374	168	126
Total		388017	800	374

Note. For the columns "# ranked" and "# rank > 3 we kept track of overlaps between searches, but not for the column "# scanned." Where there are empty fields, we have not kept track of the distinct counts.

search. There were 11,539 such systems found in the 580 tile catalogs.

For the SV data, we reprocessed the coadd tiles using the afterburner GAIN deblending technique (Zhang et al. 2014). The technique searches for blended sources that are not associated with the already cataloged objects. Searching considers image intensity peaks, image intensity gradient, and also image segmentation area. The photometry measurement is performed after evaluating the light contamination from neighboring sources. Though GAIN found only 1% more source and lens candidate objects than the DESDM algorithm, the number of lens candidates that were matched within 8″ of a

Table 2
Properties of Candidate Lensing Systems, Ordered by Increasing R.A.

System Name	Algorithm	Rank	Radius (″)	References
DESJ0004–0103	BNA, 1K, RedM	6	2.80 ± 0.29	…
DESJ0006–4208	RNA	6	8.42 ± 0.27	…
DESJ0006–4429	1K	5	2.30 ± 0.27	…
DESJ0007–4434	RNA, 1K	7	3.50 ± 0.27	…
DESJ0008–5503	1K	4	3.63 ± 0.27	…
DESJ0011+0217	BNA	3	3.71 ± 0.33	…
DESJ0011–4614	BNA, RNA, SPT, RedM, 1K	9	5.73 ± 1.05	SPT-CL J0011-4614(a)
DESJ0021–4040	RedM	4	3.14 ± 0.27	…
DESJ0021–5028	RedM, 1K	4	4.27 ± 0.46	…
DESJ0023–4923	RNA	7	4.98 ± 0.99	…
DESJ0025–4133	RedM, SPT	3	8.58 ± 0.37	…
DESJ0030–5213	RedM	3	3.59 ± 0.27	…
DESJ0031–4403	RNA	6	3.51 ± 0.27	…
DESJ0033–5445	BNA	4	4.26 ± 0.74	…
DESJ0035–5130	RedM	3	10.83 ± 3.73	…
DESJ0037–4131	BNA	8	2.42 ± 0.35	…
DESJ0040–5819	1K	3	4.40 ± 0.38	…
DESJ0040–4407	RNA, SPT	10	18.42 ± 0.27	SPT-CL J0040-4407(a)
DESJ0041–4155	BNA, RNA	9	7.23 ± 0.50	DESJ0041–4155(b)
DESJ0045–4752	RNA	4	2.41 ± 0.27	…
DESJ0047–5125	RNA	3	2.26 ± 0.27	…
DESJ0049–5414	BNA	3	2.93 ± 0.27	…
DESJ0050–5139	RedM	3	6.84 ± 0.71	…
DESJ0052–4650	RedM	6	2.56 ± 0.27	…
DESJ0053–4848	BNA, 1K	3	3.19 ± 0.27	…
DESJ0054–4636	BNA	3	3.47 ± 0.74	…
DESJ0057–4848	RNA, RedM	7	1.92 ± 0.27	…
DESJ0058–4914	BNA	3	6.69 ± 0.27	…
DESJ0101–4120	BNA	4	4.93 ± 0.27	…
DESJ0101–4713	RNA	3	8.93 ± 0.28	…
DESJ0102–4440	BNA, RNA, RedM	9	2.65 ± 0.47	…
DESJ0102–4916	RNA	10	34.81 ± 0.27	SPT-CL J0102-4915(a),(c),(d)
DESJ0104–5341	RedM	7	2.51 ± 0.27	DESJ0104–5341(b)
DESJ0104–4536	RedM	3	2.95 ± 0.48	…
DESJ0105–5058	RNA	3	2.27 ± 0.32	…
DESJ0105–4524	RedM	3	5.87 ± 0.27	…
DESJ0106–4908	1K	3	3.38 ± 1.01	…
DESJ0106–5355	BNA, RNA, SPT, RedM, 1K	10	10.66 ± 1.72	SPT-CL J0106-5355(a)
DESJ0114–4123	SPT, RedM	4	7.96 ± 0.27	…
DESJ0116–5046	RedM	3	8.12 ± 0.73	…
DESJ0118–5637	SPT	4	6.53 ± 0.27	…
DESJ0120–5143	BNA, RNA, RedM, 1K	10	3.35 ± 0.51	DESJ0120–5143(b)
DESJ0121–4459	BNA	5	2.38 ± 0.28	…
DESJ0122–5837	BNA	7	3.42 ± 0.40	…
DESJ0122–5457	BNA	4	3.30 ± 0.27	…
DESJ0123–5226	RNA	3	1.72 ± 0.27	…
DESJ0125–4142	RNA	6	1.98 ± 0.27	…
DESJ0134–4601	RNA, RedM	6	4.78 ± 2.12	…
DESJ0135–4232	RNA, 1K	10	2.21 ± 0.27	…
DESJ0138–4600	1K	3	3.72 ± 0.27	…
DESJ0142–5032	BNA, RNA, SPT, RedM	10	14.25 ± 0.89	SPT-CL J0142-5032(a)
DESJ0143–4721	BNA	5	2.49 ± 0.27	…
DESJ0143–4908	RedM	4	6.43 ± 1.36	…
DESJ0144–4523	RNA	4	2.80 ± 0.27	…
DESJ0147–4257	RedM	4	3.40 ± 0.27	…
DESJ0147–4726	RedM	4	1.92 ± 0.52	…
DESJ0148–4340	RNA	3	3.73 ± 0.59	…
DESJ0150–5527	RNA	5	2.14 ± 0.27	…
DESJ0150–5532	RNA, RedM	6	8.96 ± 1.72	…
DESJ0151–5655	SPT	5	17.25 ± 0.27	…
DESJ0157–5046	1K	4	6.90 ± 3.72	…
DESJ0158–5205	RedM	6	4.34 ± 0.27	…
DESJ0201–4109	RNA, RedM	6	3.90 ± 0.27	…
DESJ0201–4104	RedM	3	4.05 ± 0.79	…
DESJ0205–4038	BNA, RedM, 1K, RNA	8	5.81 ± 0.31	…
DESJ0205–4133	BNA	5	3.16 ± 0.30	…
DESJ0207–4553	RNA	4	5.91 ± 0.27	…
DESJ0210–4254	BNA	3	5.22 ± 0.42	…
DESJ0212–5428	1K	3	2.73 ± 0.28	…
DESJ0214–0429	BNA	4	3.07 ± 0.39	…
DESJ0219–4834	RedM, 1K	5	3.61 ± 0.27	…
DESJ0220–4056	BNA	3	5.32 ± 0.29	…

Table 2
(Continued)

System Name	Algorithm	Rank	Radius (″)	References
DESJ0222–5031	BNA, 1K	4	2.64 ± 0.27	…
DESJ0227–4516	RNA, RedM	7	4.11 ± 0.28	…
DESJ0227–4051	RedM	3	8.52 ± 1.04	…
DESJ0228–5033	RNA	6	3.62 ± 1.02	…
DESJ0230–5328	BNA, RedM	6	4.37 ± 0.43	…
DESJ0232–0323	BNA	9	3.46 ± 0.30	SDSS J0232-0323(e),(f)
DESJ0234–4529	BNA	3	3.64 ± 0.74	…
DESJ0236–5121	BNA, RNA, 1K	6	3.76 ± 1.09	…
DESJ0242–4150	SPT	3	9.49 ± 0.27	…
DESJ0243–4833	SPT	3	16.36 ± 0.27	SPT-CL 0243-4833(a)
DESJ0244–5249	1K	3	4.30 ± 1.31	…
DESJ0245–5315	RNA	4	13.74 ± 0.27	…
DESJ0245–5129	RedM	5	2.87 ± 0.72	…
DESJ0246–4544	RNA	6	3.15 ± 0.40	…
DESJ0247–5917	1K	7	3.22 ± 0.27	…
DESJ0249–0048	1K	5	3.40 ± 0.27	…
DESJ0249–5446	1K	4	2.67 ± 0.27	…
DESJ0251–5515	RedM, 1K	6	7.04 ± 0.27	…
DESJ0252–4732	RNA, RedM	6	2.85 ± 0.27	…
DESJ0254–4044	BNA	4	4.92 ± 0.40	…
DESJ0255–4807	RNA	3	2.06 ± 0.44	…
DESJ0257–5843	1K	4	6.97 ± 0.60	…
DESJ0259–4555	RNA, SPT, RedM	5	5.55 ± 0.27	…
DESJ0300–5001	RedM	8	7.75 ± 0.62	…
DESJ0300–5144	RedM	5	2.55 ± 0.27	…
DESJ0300–4941	RNA	3	17.93 ± 0.27	…
DESJ0303–5805	RedM	3	4.73 ± 0.27	…
DESJ0303–5704	RedM	3	14.43 ± 1.03	…
DESJ0303–4626	RNA	5	3.07 ± 0.75	…
DESJ0303–4842	RedM	3	4.75 ± 0.27	…
DESJ0304–4921	RNA, SPT, RedM	10	24.88 ± 0.49	SPT-CL J0304-4921(a), (g)
DESJ0305–4625	RedM	3	3.81 ± 0.27	…
DESJ0306–4149	1K	5	3.00 ± 0.27	…
DESJ0307–5042	RNA, SPT, RedM, 1K	7	10.51 ± 1.88	SPT-CL J0307-5042(a)
DESJ0310–4534	RNA	6	3.00 ± 0.38	…
DESJ0310–4450	RedM	4	3.32 ± 0.27	…
DESJ0310–4647	RNA, SPT, RedM, 1K	9	9.55 ± 0.44	SPT-CL J0310-4647(a)
DESJ0312–5621	1K	6	7.74 ± 0.27	…
DESJ0313–4337	RNA	5	3.73 ± 0.27	…
DESJ0313–4633	BNA	6	3.43 ± 0.42	…
DESJ0316–4816	BNA	3	3.01 ± 0.44	…
DESJ0318–4306	BNA	6	3.98 ± 0.85	…
DESJ0318–4818	RedM	6	3.72 ± 0.27	…
DESJ0319–5318	RedM	3	3.46 ± 0.27	…
DESJ0319–4455	BNA	5	2.65 ± 0.34	…
DESJ0322–5234	RedM	9	3.67 ± 0.27	…
DESJ0325–5607	BNA	3	3.03 ± 0.28	…
DESJ0326–5645	RNA	6	2.27 ± 0.33	…
DESJ0327–5142	BNA	3	2.29 ± 0.27	…
DESJ0330–5228	RNA, SPT, RedM	10	6.08 ± 0.88	SPT-CL J0330-5228(a),(g),(h)
DESJ0331–2713	BNA	3	6.61 ± 0.27	…
DESJ0332–5836	RedM	5	3.91 ± 1.09	…
DESJ0333–5842	SPT, RedM	5	6.51 ± 0.27	…
DESJ0334–4817	RedM	4	3.26 ± 0.27	…
DESJ0338–4909	RedM	3	1.77 ± 0.27	…
DESJ0339–4849	RNA, RedM	6	10.51 ± 0.89	…
DESJ0339–4800	RedM	4	2.20 ± 0.27	…
DESJ0341–5130	RedM, 1K	6	2.35 ± 0.27	…
DESJ0342–5355	RNA, SPT	8	4.75 ± 0.39 (1, 2) 10.88 ± 0.63 (3, 4)	…
DESJ0342–5504	RedM	4	9.21 ± 0.27	…
DESJ0343–5518	RNA, SPT, RedM	6	13.77 ± 1.15	…
DESJ0344–5828	BNA	3	4.53 ± 0.47	…
DESJ0345–4112	RedM	3	9.54 ± 1.19	…
DESJ0346–5018	RNA, RedM	5	4.91 ± 0.38	…
DESJ0346–6158	RedM	6	2.92 ± 0.27	…
DESJ0347–4535	BNA	7	3.39 ± 0.38	…
DESJ0348–5350	RedM	3	14.42 ± 0.27	…
DESJ0349–4857	BNA, 1K	8	6.16 ± 0.85	…
DESJ0349–4454	RNA, RedM	6	4.06 ± 0.74	…
DESJ0351–5637	RedM	4	12.36 ± 1.36	…
DESJ0352–4928	RNA, RedM	6	3.38 ± 0.68	…

Table 2
(Continued)

System Name	Algorithm	Rank	Radius (″)	References
DESJ0352–5647	SPT	6	10.79 ± 0.36	…
DESJ0353–4024	RNA	6	3.22 ± 0.27	…
DESJ0354–4446	RedM	3	3.14 ± 0.27	…
DESJ0357–4756	RedM	9	8.09 ± 2.20	DESJ0357–4756(b)
DESJ0357–4100	BNA	3	2.99 ± 0.27	…
DESJ0357–5810	RNA, RedM	6	4.64 ± 0.27	…
DESJ0358–5436	BNA	6	3.47 ± 0.32	…
DESJ0358–5009	RedM	3	25.69 ± 4.93	…
DESJ0400–5331	BNA	3	3.00 ± 0.27	…
DESJ0400–6400	BNA	3	1.71 ± 0.28	…
DESJ0400–4229	RNA	4	4.19 ± 0.31	…
DESJ0401–4753	RedM	3	7.52 ± 0.27	…
DESJ0402–5837	BNA, 1K	4	8.25 ± 0.46	…
DESJ0402–5258	RedM	3	2.86 ± 0.27	…
DESJ0403–5057	RNA	8	2.37 ± 0.35	…
DESJ0405–6418	BNA	4	4.36 ± 0.43	…
DESJ0405–4915	RedM	3	17.22 ± 8.32	…
DESJ0406–5023	1K	4	5.89 ± 0.27	…
DESJ0407–6455	BNA	4	2.02 ± 0.50	…
DESJ0408–5353	RedM, 1K	6	2.41 ± 0.56	DESJ0408–5353(i)
DESJ0408–5327	RNA	10	3.02 ± 0.41	…
DESJ0409–6510	1K	4	1.60 ± 0.27	…
DESJ0411–4506	BNA	3	4.24 ± 0.27	…
DESJ0411–4819	RNA, SPT	10	7.13 ± 0.60	SPT-CL J0411-4819(a)
DESJ0412–5659	RNA	6	5.17 ± 0.72	…
DESJ0412–4258	RNA	5	1.84 ± 0.45	…
DESJ0416–6212	RNA	3	2.85 ± 0.72	…
DESJ0416–5525	RedM, 1K	3	4.21 ± 0.27	…
DESJ0418–4954	1K	3	2.65 ± 0.27	…
DESJ0418–5457	BNA, 1K	8	1.97 ± 0.27	DESJ0418–5457(b)
DESJ0419–5527	BNA	3	3.22 ± 0.69	…
DESJ0423–4610	RedM	3	6.42 ± 0.36	…
DESJ0423–5431	RedM, 1K	6	4.61 ± 0.27	…
DESJ0426–4104	RedM	4	3.71 ± 0.27	…
DESJ0429–6233	RNA	5	2.05 ± 0.27	…
DESJ0430–5030	RedM	3	2.23 ± 0.27	…
DESJ0434–4943	RedM	3	10.52 ± 0.27	…
DESJ0434–5138	RNA	6	3.14 ± 0.38	…
DESJ0436–5636	RedM	3	9.67 ± 0.27	…
DESJ0439–5533	RedM	5	5.93 ± 1.41	…
DESJ0440–4657	RedM, SPT	7	8.17 ± 0.27	…
DESJ0441–4855	SPT	4	13.34 ± 0.27	SPT-CL J0441-4855(a)
DESJ0443–4457	RedM	5	6.67 ± 0.27	…
DESJ0444–4542	RNA, RedM	6	5.30 ± 1.57	…
DESJ0445–5114	RNA	3	2.02 ± 0.27	…
DESJ0445–4303	RedM	3	3.89 ± 0.27	…
DESJ0445–4406	RNA, RedM	6	3.47 ± 0.27	…
DESJ0445–4344	1K	3	3.72 ± 0.51	…
DESJ0445–4343	RedM	4	9.99 ± 0.27	…
DESJ0446–5126	RedM	3	7.61 ± 1.26	DESJ0446–5126(h)
DESJ0446–5318	RedM	3	2.61 ± 0.27	…
DESJ0446–6349	RNA	4	1.39 ± 0.27	…
DESJ0448–5807	RedM	3	2.73 ± 0.27	…
DESJ0449–5857	RNA	4	5.49 ± 0.39	…
DESJ0450–5715	RNA	9	2.60 ± 0.27	…
DESJ0451–4202	RedM	4	5.62 ± 0.31	…
DESJ0451–5311	RedM	3	5.27 ± 1.42	…
DESJ0453–5824	RNA	3	2.70 ± 0.27	…
DESJ0454–5714	1K	5	1.56 ± 0.27	…
DESJ0454–4252	RNA	4	2.15 ± 0.30	…
DESJ0455–6128	RedM	3	5.05 ± 0.56	…
DESJ0456–6224	RNA	6	3.37 ± 0.27	…
DESJ0457–4531	RedM	3	4.40 ± 0.27	…
DESJ0502–6113	RNA, SPT, RedM	7	5.21 ± 1.00	…
DESJ0502–5448	RNA	4	2.79 ± 0.27	…
DESJ0503–5052	RedM	5	3.42 ± 0.27	…
DESJ0503–5658	1K	3	4.47 ± 0.27	…
DESJ0509–5342	BNA, SPT	6	9.44 ± 1.02	SPT-CL J0509-5342(a),(g),(j)
DESJ0509–5227	RNA	6	3.86 ± 0.27	…
DESJ0510–5637	RedM, 1K	6	3.60 ± 0.56	…
DESJ0510–4151	BNA	3	6.69 ± 0.97	…
DESJ0510–5207	BNA	3	3.79 ± 0.32	…

Table 2
(Continued)

System Name	Algorithm	Rank	Radius (″)	References
DESJ0512–5652	RNA	3	2.48 ± 0.47	…
DESJ0512–5041	RedM	4	3.79 ± 0.27	…
DESJ0514–5142	BNA, RNA, RedM	5	5.32 ± 0.27	…
DESJ0514–6226	BNA	3	2.34 ± 0.29	…
DESJ0514–5626	RNA	3	1.97 ± 0.27	…
DESJ0516–6312	SPT	4	10.50 ± 0.27	…
DESJ0516–4940	BNA	3	1.88 ± 0.31	…
DESJ0518–5720	1K	7	4.59 ± 0.27	…
DESJ0522–4204	RedM	6	8.30 ± 0.27	…
DESJ0525–5447	BNA	5	2.55 ± 0.28	…
DESJ0525–4424	RNA	9	2.94 ± 0.27	…
DESJ0528–6033	BNA	6	2.06 ± 0.33	…
DESJ0530–5447	RedM, 1K	5	5.25 ± 0.27	…
DESJ0534–5446	RNA	3	3.24 ± 0.84	…
DESJ0536–5338	RNA, RedM	6	3.42 ± 0.84	…
DESJ0537–6504	SPT	3	4.61 ± 0.27	…
DESJ0537–4711	BNA	4	6.38 ± 0.27	…
DESJ0538–5923	BNA	6	1.91 ± 0.33	…
DESJ0538–4735	RNA, RedM	6	2.14 ± 0.42	…
DESJ0538–4022	RNA	6	2.54 ± 0.31	DESJ0538–4022(b)
DESJ0541–4234	RNA, RedM	6	5.22 ± 0.27	…
DESJ0541–5143	RedM	3	4.73 ± 0.40	…
DESJ0547–6004	1K	5	4.14 ± 0.71	…
DESJ0548–4503	RedM	4	3.61 ± 0.58	…
DESJ0549–6206	RNA	5	9.12 ± 0.27	…
DESJ0549–6205	RNA	7	18.49 ± 0.27	…
DESJ0549–5008	RNA	6	8.63 ± 0.61	…
DESJ0553–4001	1K	6	7.35 ± 0.91	…
DESJ0556–5403	RNA	4	4.44 ± 0.29	…
DESJ0557–4113	RNA	6	15.46 ± 0.27	…
DESJ0558–5010	RNA	5	2.37 ± 0.29	…
DESJ0602–4653	RedM	6	2.03 ± 0.27	…
DESJ0602–4524	BNA, 1K	10	3.13 ± 0.27	…
DESJ0603–5238	RedM	5	3.40 ± 0.27	…
DESJ0604–4613	RedM	4	2.98 ± 0.27	…
DESJ0607–5436	RedM	6	7.33 ± 0.27	…
DESJ0607–5733	RNA, RedM	6	3.39 ± 0.27	…
DESJ0608–4031	RedM	6	7.26 ± 0.27	…
DESJ0609–5926	RedM	3	3.54 ± 0.27	…
DESJ0610–4039	RedM	5	6.04 ± 0.27	…
DESJ0610–4053	RNA	3	5.40 ± 0.27	…
DESJ0610–5559	RNA	8	4.00 ± 0.27 (1)	…
			9.25 ± 0.44 (2, 3)	
DESJ0611–5936	RedM	3	2.44 ± 0.27	…
DESJ0611–5905	RNA, RedM	5	9.37 ± 0.27	…
DESJ0611–5514	RedM	6	7.63 ± 1.40	…
DESJ0612–5611	1K	4	2.06 ± 0.27	…
DESJ0613–4208	RedM	3	3.51 ± 0.27	…
DESJ0614–4604	RedM	3	14.02 ± 0.27	…
DESJ0620–6137	BNA	6	4.03 ± 0.51	…
DESJ0625–4526	BNA	6	1.88 ± 0.27	…
DESJ0655–5523	BNA	3	4.03 ± 0.80	…
DESJ0657–5543	BNA	6	3.18 ± 0.27	…
DESJ0658–5556	RNA, SPT, 1K	10	7.66 ± 2.97	1E0657-56/Bullet Cluster(a),(k)
DESJ0658–5558	RNA	7	12.26 ± 0.27	…
DESJ0702–5529	1K	4	4.92 ± 0.27	…
DESJ1956–5751	RNA	4	2.01 ± 0.46	…
DESJ2011–5228	RNA, SPT	10	10.64 ± 4.71	SPT-CL J2011-5228(a),(l),(m)
DESJ2016–4954	SPT, RedM, 1K	6	12.20 ± 1.98	…
DESJ2022–5448	BNA	3	3.38 ± 0.28	…
DESJ2025–5117	SPT	4	6.40 ± 0.27	…
DESJ2030–5538	RedM	6	3.16 ± 0.27	…
DESJ2037–5601	RNA	6	3.32 ± 0.38	…
DESJ2039–5459	BNA, RNA, RedM, 1K	8	3.04 ± 0.64	…
DESJ2048–5747	1K	3	4.47 ± 0.73	…
DESJ2048–5507	BNA	3	2.74 ± 0.27	…
DESJ2050–5907	BNA	3	6.92 ± 0.92	…
DESJ2052–5822	RNA	6	9.45 ± 0.41	…
DESJ2056–5213	BNA	3	3.61 ± 1.07	…
DESJ2102–5825	1K	4	3.89 ± 0.27	…
DESJ2110–5639	1K	6	2.88 ± 0.27	…

Table 2
(Continued)

System Name	Algorithm	Rank	Radius (″)	References
DESJ2111–0114	RNA, RedM	9	11.55 ± 1.45	SDSS J2111-0114(f),(n),(o)
DESJ2113–0114	BNA, RedM, 1K	6	2.42 ± 0.27	DESJ2113–0114(b)
DESJ2114+0002	BNA	3	2.14 ± 0.39	…
DESJ2115–5838	RNA	7	2.63 ± 0.27	…
DESJ2116–5704	BNA	3	3.83 ± 0.51	…
DESJ2119+0030	1K	4	10.53 ± 0.27	…
DESJ2122–0059	RedM, 1K	8	3.46 ± 0.27	…
DESJ2123–5053	RedM	3	3.20 ± 0.27	…
DESJ2124–0133	RNA, RedM	6	11.24 ± 0.44	…
DESJ2127–5149	BNA, RedM, 1K	9	4.74 ± 0.54	…
DESJ2135–5727	BNA	3	2.19 ± 0.27	…
DESJ2137–5154	RedM	3	4.43 ± 0.27	…
DESJ2138–5838	RedM	5	3.32 ± 0.85	…
DESJ2140+0057	BNA	3	5.61 ± 0.34	…
DESJ2141–5201	RedM, 1K	5	5.33 ± 0.27	…
DESJ2145–5501	RedM	5	5.65 ± 0.33	…
DESJ2149–0012	RedM	6	3.13 ± 0.27	…
DESJ2151–5406	RedM	3	4.18 ± 0.36	…
DESJ2156+0123	RedM	3	13.90 ± 0.27	…
DESJ2156+0058	RNA	5	6.90 ± 0.77	…
DESJ2157–5700	RedM	4	4.84 ± 0.27	…
DESJ2159–5209	RNA, RedM	6	4.89 ± 0.28	…
DESJ2159+0026	1K	3	2.36 ± 0.27	…
DESJ2207–5541	BNA	3	2.92 ± 0.27	…
DESJ2208–0124	BNA	4	2.93 ± 0.27	…
DESJ2209–5729	BNA	3	1.39 ± 0.27	…
DESJ2209–5109	RNA	4	10.19 ± 0.27	…
DESJ2210–5554	BNA	3	5.90 ± 0.27	…
DESJ2212–0008	BNA, RNA, RedM	7	3.73 ± 0.75	…
DESJ2213–0018	RNA, RedM	4	6.49 ± 1.01	…
DESJ2214+0110	RNA	4	3.60 ± 0.62	SL2S J221419+011034(f),(p)
DESJ2215+0102	RedM	4	2.49 ± 0.27	…
DESJ2219–5040	BNA	3	2.89 ± 1.11	…
DESJ2219–5816	RedM	6	4.07 ± 0.27	…
DESJ2223–5223	RNA	5	3.99 ± 0.41	…
DESJ2224–5144	RNA	3	2.45 ± 0.32	…
DESJ2226+0041	1K	7	2.27 ± 0.27	HSCJ222609+004141(q)
DESJ2231–5838	BNA	3	1.80 ± 0.28	…
DESJ2231–5844	RNA	6	6.61 ± 0.27	…
DESJ2232–5807	RNA, RedM	6	8.06 ± 0.27	…
DESJ2237–5030	RedM	3	6.28 ± 0.27	…
DESJ2239–5453	1K	4	2.71 ± 0.27	…
DESJ2240–4258	RNA, RedM	7	6.38 ± 1.06	…
DESJ2240–5245	RedM	7	5.82 ± 0.27	…
DESJ2241–0057	BNA	5	2.94 ± 0.46	…
DESJ2247–4821	RedM	5	4.42 ± 0.49	…
DESJ2248–4819	RedM	3	2.91 ± 0.27	…
DESJ2248–4431	RNA, RedM, SPT	9	28.52 ± 4.25	AS1063(a),(r)
DESJ2249–0110	RedM	4	4.07 ± 0.27	…
DESJ2250–5345	RedM	6	5.87 ± 1.01	…
DESJ2250–5311	RedM	4	2.15 ± 0.27	…
DESJ2251–4412	RNA	5	3.41 ± 0.28	…
DESJ2252+0107	BNA	3	4.45 ± 0.27	…
DESJ2253–4517	RedM, 1K	6	9.67 ± 0.27	…
DESJ2254–4055	1K	6	1.44 ± 0.27	…
DESJ2254–4620	RNA, SPT	8	31.13 ± 2.21	…
DESJ2255–4708	RedM	4	2.70 ± 0.27	…
DESJ2255–5225	1K	3	3.01 ± 0.27	…
DESJ2258–4811	RNA	5	9.58 ± 0.27	…
DESJ2300–5820	RedM	5	7.52 ± 0.74	…
DESJ2304–4054	RedM	4	2.05 ± 0.27	…
DESJ2306–4043	BNA	3	4.60 ± 0.27	…
DESJ2306–4931	1K	3	3.58 ± 0.27	…
DESJ2307–5440	BNA, RedM	4	8.64 ± 0.27	…
DESJ2307+0106	BNA	3	2.64 ± 0.29	…
DESJ2308+0008	RedM	3	2.82 ± 0.29	…
DESJ2309–0047	BNA	3	3.01 ± 0.34	…
DESJ2310–5108	BNA	3	3.92 ± 0.32	…
DESJ2311–5522	RedM	3	5.91 ± 0.27	…
DESJ2312–0117	RedM	4	3.03 ± 0.27	…
DESJ2313–0104	RNA, RedM	7	6.94 ± 0.54	…
DESJ2319–4436	BNA	4	6.40 ± 0.29	…

Table 2
(Continued)

System Name	Algorithm	Rank	Radius (″)	References
DESJ2321–4630	BNA, RedM, 1K, RNA	10	3.47 ± 0.63	DESJ2321–4630(b)
DESJ2324–4944	RNA, RedM	6	4.87 ± 0.28	…
DESJ2325–4111	SPT	9	9.62 ± 1.25	SPT-CL J2325-4111(a)
DESJ2328–5206	BNA	5	3.24 ± 0.68	…
DESJ2328–0030	BNA	5	3.41 ± 0.29	…
DESJ2329–0120	RedM, 1K	6	5.91 ± 0.27	…
DESJ2332–5358	RedM	3	12.64 ± 0.27	SPT-CL J2332-5358(a),(s),(t)
DESJ2335–5152	RNA, 1K	8	3.90 ± 0.27	…
DESJ2336–5352	BNA, RNA, RedM, 1K	10	5.96 ± 1.44	DESJ2336–5352(h)
DESJ2347–4616	1K	3	3.71 ± 0.27	…
DESJ2349–5113	RedM	9	4.30 ± 0.57	DESJ2349–5113(b)
DESJ2351–5032	RedM	3	3.55 ± 0.27	…
DESJ2351–5452	RNA, SPT	10	7.11 ± 0.97	SPT-CL J2351-5452(a),(u),(v)
DESJ2355–0007	RNA	4	2.08 ± 0.27	…
DESJ2356–5057	RNA, RedM, 1K	3	14.23 ± 1.17	…
DESJ2356+0012	RedM	3	6.00 ± 1.10	…
DESJ2359–5245	BNA	5	5.29 ± 0.57	…

Note. Names, algorithms that detected the system, the visual inspection rank, average radius, and references to detections in other papers. The names match those that label the system images in the panels in Figures 6–16. The algorithms are as follows: BNA ≡ BNA 2+; 1K ≡ BNA 1K; RedM ≡ redMaPPer clusters and redMaGiC galaxies; SPT ≡ SPT clusters; RNA ≡ red near anything.

References. (a) Bleem et al. (2015), (b) B. Nord et al. (2017, in preparation), (c) Menanteau et al. (2012), (d) Zitrin et al. (2013), (e) Stark et al. (2013), (f) L. Moustakas & J. Brownstein (2017, in preparation), (g) Menanteau et al. (2010a), (h) Nord et al. (2016), (i) Lin et al. (2017), (j) Staniszewski et al. (2009), (k) Mehlert et al. (2001), (l) Song et al. (2012), (m) Collett et al. (2017), (n) Bayliss et al. (2011), (o) Hennawi et al. (2008), (p) More et al. (2012), (q) Sonnenfeld et al. (2017), (r) Gómez et al. (2012), (s) Greve et al. (2012), (t) Aravena et al. (2013), (u) Menanteau et al. (2010b), (v) Buckley-Geer et al. (2011).

(This table is available in machine-readable form.)

source candidate was 4% higher and there were more source matches per lens candidate. Repeating the BNA algorithm resulted in the identification of 14,258 candidate lens systems. We removed candidate SL systems identified in the GAIN catalogs that were within 10″ of any candidate system identified in the DESDM catalogs. A total of 3281 candidate lens systems remained.

The BNA algorithm used for Y1A1 was similar to that used for SV. There were minor changes for the first pass through the data. The criteria to eliminate both artifacts from the list of lens and source candidates was strengthened. A total of 43,598 systems were identified that had at least two or more matched source objects. These were scanned for lens systems as described above. Later we ran the BNA algorithm again, this time with the source and lens object magnitude limits raised from 21.0 to 21.5. This time a total of 74,624 systems were identified. Removing any within 10″ of the previous list (of 43,598) left 31,964 candidate lens systems to scan. The combination of these two Y1A1 2+ knot searches yielded 211 candidates in the SL short list. Of these, 96 had a rank of 3 or above.

Having noticed that our BNA 2+ search was vulnerable to missing systems where only one source object had been identified, we implemented a search for "One Knot" lens candidates, referred to as BNA 1K. In order to leave a list of candidates that were short enough to scan, we applied more restrictive criteria to the lens and source object selection. In addition to the criteria listed for the BNA algorithm, we required that candidate lens objects contain at least one half of their $i-band$ flux within a radius of $<1\farcs84$ (7 pixels), have a ratio of the length of the major-to-minor axis <7, and that $g-r>0.7$ and $r-i>0.3$. The cuts on the flux radius and major-to-minor axis ratio remove artifacts such as diffraction spikes from stars, satellite trails, and deblended pieces of large nearby galaxies. Finally, we required that the magnitude for the r-band, i-band, or z-band be less than 20. These criteria restricted the lens list to bright red galaxies. The source list selection criteria was the same as in the BNA algorithm, but with the magnitude limited to objects brighter than 20.5 in the g, r, or i-bands. The maximum matching radius was reduced to 6″. Finally, we eliminated the fainter of any system that was within 10″ of any other system. The SV data yielded 35,012 candidates. This was reduced to 18,010 for scanning by requiring that the lens system be north of decl. $=-60°$ to avoid the crowded Large Magellanic Cloud. There were 132,725 candidates in Y1A1 and it was not necessary to require that they were north of decl. $=-60°$ because we had stayed away from the Large Magellanic Cloud during the Y1 observations. The BNA 1K searches added an additional 14 systems from SVA1 and 107 systems from Y1A1 to the short list. The other searches described here had not identified 81 of these. The combined SV plus Y1 BNA 1K searches yielded 75 systems with a rank of 3 or more. Of these, 36 were uniquely discovered by the BNA 1K search.

The combined BNA 2+ and BNA 1K searches formed a final BNA list of 153 SL candidates with a rank of 3 or more. Their mean rank was 4.9 (out of 10).

3.3. Search around redMaPPer Galaxy Clusters and redMaGiC Galaxies

We searched for strong lens candidates at the location of galaxy clusters identified by the redMaPPer technique (Rykoff et al. 2014). redMaPPer was used to produce a catalog of galaxy clusters where the richness, defined as the sum of the membership probability of every galaxy in the cluster field (Rozo et al. 2009), was greater than 20. The search of 786 such clusters (Rykoff et al. 2016) in SVA1 has been previously described (Nord et al. 2016). Here, we present

the results from the search of 7,328 redMaPPer clusters from Y1A1.

We also searched the DES Y1A1 LRG sample selected using the redMaGiC technique (Rozo et al. 2016), which lists 3M galaxies. Most stellar contaminants were removed from the lensing galaxy sample using a selection criterion from the SExtractor output. We then identified as our initial set of 6,526 candidates those redMaGiC galaxies with three or more blue (source) objects within a radius $<10''$, where we defined a blue object as one with colors $-1 \leqslant g - r < 1$ and $-1 \leqslant r - i < 1$. We did not apply any star/galaxy separation cut to the blue objects, but did require that the objects were not poorly deblended or contained saturated pixels in each of the g, r, i-band filters. We also applied a magnitude cut $r < 22$ on the blue objects in order to keep the number of candidates manageable for the visual inspection step, as well as to have relatively brighter candidates to ease follow-up spectroscopic redshift measurements. Systems not already identified in the redMaPPer search were added to the SL candidate short list.

The combined redMaGic and redMapper searches (referred to as RedM) yielded 374 candidates to the SL candidate short list. Of these, 170 had a final rank of 3 or higher after final selection. The mean rank for those 170 systems was 5.1 (out of 10).

3.4. "Red Near Anything Knot" Searches

This is a knot search intended to discover systems with red-colored sources, referred to as RNA. It was similar to the BNA search used for Y1A1 (described above), except as noted, in that a list of source candidates was matched against a list of lens candidates with an $8''$ maximum radius. There were two main iterations of this campaign. In both of them, the lens candidate selection criteria was the same as those used the for BNA algorithm, namely any of $r, i, z < 21.5$. In both iterations, there were two selection criteria for the source lists. The first was that any of $r, i, z < 21.5$, that $g > 23$, and that $g - r > 0$ and $r - i > 0$. The second was that any of $r, i, z < 21.5$ (as in the first), that $g > 23$ and $r > 23$, and that $r - i > 0$ and $i - z > 0$. In the first iteration, we found that largest set of matching sources for which $|\Delta(g - r)| < 0.25$ and $|\Delta(r - i)| < 0.25$. For the SV data, we visually scanned the 3091 candidate lens systems with 3 or more matching sources with decl. $> -62.^{\circ}5$, again avoiding the Large Magellanic Cloud. For the Y1A1 data we visually scanned 67,179 candidate lens systems with two or more matching sources.

We carried out the second iteration of this campaign on the Y1A1 data after we realized that the color-matching selection criterion $|\Delta(g - r)| < 0.25$ would eliminate source objects that were g and r-band dropouts. So we reran the algorithm, this time requiring that $|\Delta(r - i)| < 0.25$ and $|\Delta(i - z)| < 0.25$. That provided a list of 122,712 candidate systems with two or more color-matched sources. Of these, 117,178 were north of decl. $= -60^{\circ}$, and 56,570 of those were not within $10''$ of a system visually scanned in the first campaign. So we visually scanned the disjoint set. Finally, we searched the 5,534 candidates that were south of decl. $= -60^{\circ}$.

In total, we visually scanned more than 132,000 RNA candidate systems. There were 168 short-listed candidates. This was finally reduced to 126 systems with a rank of 3 or higher, for which the mean rank was 6.1 (out of 10). Most of the candidate systems found by this search contained closely spaced luminous red galaxies, though there were a few with red-colored sources.

4. Search Results

The ranked lists from the various searches were combined. We identified 374 lens system candidates with a ranking of 3 or greater. A total of 348 are presented for the first time. Figure 4 contains a histogram of the rank for the systems that had a rank of 3 or more. We found some candidate systems in more than one search; with some systems being identified in every search that we performed. Figure 5 shows the Venn diagram of the systems indicating the overlap between the search techniques. Table 1 shows the number of objects searched, scanned, and found.

Table 2 provides the system name, the algorithms that identified the candidates for scanning, the rank as given by the experts, the distance (radius) of the source(s) from the presumed lens center, and other names for the system from previous references to it. Figures 6–16 show a 3-color cutout of each system. At the top of each image is a unique label, formed from the position, for each system. The most prominent galaxy, with the source(s) centered on it, is taken as the lens. The putative lens is centered in the image and is labeled with a letter "A." There are some systems where there is not a single galaxy to assign as the principal lens. For those systems we labeled the additional lensing objects with additional letters, e.g.,: "B," or "C." All of the lens objects are found in the DESDM SV and/or Y1A1 catalogs. Source objects are labeled on the cutout images with numbers, e.g.,: "1," "2," etc. Because it was not required that the potential sources or lenses that we identified be part of the selection that caused the system to be selected for scanning in the first place, some systems have no sources identified in the DESDM catalog. In addition, some objects may not have been in the catalog because of problems with the deblending noted in Section 2. Many of these missing sources are also identified by the number on the cutout so that the reason for the ranking is made apparent. Table 3 shows details, extracted from the catalog, for each object identified in each system for the first two pages (out of many) of systems. The full table is provided as a supplemental file, as is a copy of Table 2. These details include the identification mark on the cutout, the R.A., decl., g, r, i, z, and Y-band magnitudes (not corrected for Galactic extinction), and the photometric redshift (corrected for Galactic extinction). For those sources where there is no catalog information available, we supply the R.A. and decl. only.

Photometric redshifts (photo-z's) were computed using the "DESDM" artificial neural network method, as originally described in Oyaizu et al. (2008a, 2008b) and later vetted on DES data by Sánchez et al. (2014). The photometric redshift distributions for the lenses and for the sources are plotted in Figure 17. We expect that the lens photo-z's should be reasonably well-estimated, given that our lens samples consist predominantly of red galaxies, which have strong 4000 Å break features that yield better photo-z measurements. However, we caution that our sources, which are typically fainter blue objects, will have photo-z's that are subject to larger uncertainties. An important factor is that imperfect object deblending in these candidate lensing systems (where objects tend to be close in angular separation) will result in photometry errors that affect the photo-z measurements for the fainter sources more than those for the brighter lenses. Moreover, the

Figure 6. First page of SL systems with ranks of 3 or more. Each cutout image has the visual inspection ranking displayed in a red box in the lower right hand corner. All images are oriented with north up and east left. Most of the cutouts are $30'' \times 30''$ in size. Some of the largest systems are displayed with $60'' \times 60''$ images, so that they fit well within the cutout. A scale bar $10''$ long is displayed in the lower left hand corner.

Table 3
Names, Positions, Photometry, and Photometric Redshifts of Objects for Each Candidate Lensing System

System Name (Object Label)	R.A. (J2000)	Decl. (J2000)	(*g*, *r*, *i*, *z*, *Y*)	$z_{\rm photo}$
DESJ0004–0103 (A)	1.215538	−1.055084	(21.46 ± 0.02, 20.65 ± 0.02, 20.17 ± 0.02, 19.89 ± 0.03, 19.66 ± 0.05)	0.57 ± 0.11
DESJ0004–0103 (1)	1.215325	−1.055798	(20.32 ± 0.01, 20.18 ± 0.01, 20.12 ± 0.02, 20.08 ± 0.03, 19.89 ± 0.06)	0.34 ± 0.06
DESJ0004–0103 (2)	1.214778	−1.055363	(21.54 ± 0.01, 21.25 ± 0.01, 21.08 ± 0.02, 21.00 ± 0.04, 21.04 ± 0.08)	0.45 ± 0.06
DESJ0006–4208 (A)	1.513033	−42.136973	(22.93 ± 0.27, 20.87 ± 0.05, 19.69 ± 0.03, 19.11 ± 0.04, 18.66 ± 0.07)	0.82 ± 0.03
DESJ0006–4208 (1)	1.512545	−42.139283	(22.63 ± 0.10, 22.30 ± 0.09, 21.98 ± 0.11, 22.03 ± 0.30, 21.45 ± 0.42)	0.32 ± 0.10
DESJ0006–4429 (A)	1.685922	−44.497351	(20.21 ± 0.01, 19.19 ± 0.01, 18.64 ± 0.01, 18.31 ± 0.01, 18.12 ± 0.02)	0.47 ± 0.05
DESJ0006–4429 (1)	1.6851	−44.4971	…	…
DESJ0007–4434 (A)	1.872012	−44.579494	(20.60 ± 0.02, 18.91 ± 0.01, 18.17 ± 0.01, 17.77 ± 0.01, 17.59 ± 0.01)	0.52 ± 0.04
DESJ0007–4434 (1)	1.870954	−44.578879	(21.55 ± 0.03, 20.68 ± 0.02, 20.11 ± 0.02, 19.75 ± 0.02, 19.56 ± 0.06)	0.63 ± 0.13
DESJ0008–5503 (A)	2.067195	−55.066309	(19.90 ± 0.02, 18.53 ± 0.01, 18.05 ± 0.01, 17.76 ± 0.01, 17.61 ± 0.02)	0.28 ± 0.03
DESJ0008–5503 (1)	2.068835	−55.065944	(21.04 ± 0.05, 20.21 ± 0.03, 20.00 ± 0.04, 19.66 ± 0.04, 19.46 ± 0.10)	0.26 ± 0.11
DESJ0011+0217 (A)	2.772767	2.288907	(22.21 ± 0.04, 20.57 ± 0.01, 19.91 ± 0.01, 19.55 ± 0.01, 19.32 ± 0.05)	0.45 ± 0.03
DESJ0011+0217 (1)	2.772902	2.289994	(22.20 ± 0.03, 21.46 ± 0.02, 21.19 ± 0.03, 20.98 ± 0.04, 20.72 ± 0.14)	0.34 ± 0.13
DESJ0011+0217 (2)	2.772275	2.289742	(22.90 ± 0.06, 22.15 ± 0.06, 21.83 ± 0.06, 21.81 ± 0.09, 21.38 ± 0.30)	0.40 ± 0.10
DESJ0011+0217 (3)	2.771735	2.288908	(22.00 ± 0.04, 21.20 ± 0.04, 20.96 ± 0.04, 20.93 ± 0.07, 20.30 ± 0.18)	0.38 ± 0.12
DESJ0011–4614 (A)	2.971361	−46.239435	(21.03 ± 0.02, 19.63 ± 0.01, 18.82 ± 0.01, 18.40 ± 0.01, 18.21 ± 0.02)	0.58 ± 0.05
DESJ0011–4614 (1)	2.973613	−46.239201	(22.42 ± 0.06, 21.47 ± 0.05, 20.70 ± 0.04, 20.39 ± 0.05, 20.17 ± 0.11)	0.74 ± 0.05
DESJ0011–4614 (2)	2.972983	−46.238663	(21.27 ± 0.04, 20.61 ± 0.05, 19.95 ± 0.05, 19.52 ± 0.05, 19.37 ± 0.11)	0.99 ± 0.13
DESJ0011–4614 (3)	2.969506	−46.238942	(21.18 ± 0.03, 20.58 ± 0.04, 20.07 ± 0.04, 19.61 ± 0.05, 19.45 ± 0.09)	1.06 ± 0.13
DESJ0011–4614 (4)	2.972894	−46.241202	(21.70 ± 0.05, 20.68 ± 0.05, 20.15 ± 0.05, 19.80 ± 0.06, 19.67 ± 0.12)	0.37 ± 0.10
DESJ0021–4040 (A)	5.391826	−40.66717	(20.80 ± 0.02, 19.30 ± 0.01, 18.61 ± 0.01, 18.21 ± 0.01, 18.04 ± 0.02)	0.54 ± 0.05
DESJ0021–4040 (1)	5.3912	−40.6679	…	…
DESJ0021–5028 (A)	5.452791	−50.476023	(20.70 ± 0.01, 19.04 ± 0.01, 18.47 ± 0.01, 18.18 ± 0.01, 18.03 ± 0.02)	0.35 ± 0.05
DESJ0021–5028 (1)	5.454056	−50.475302	(21.43 ± 0.02, 20.66 ± 0.02, 20.31 ± 0.03, 20.17 ± 0.05, 19.83 ± 0.09)	0.28 ± 0.08
DESJ0021–5028 (2)	5.451831	−50.474888	(23.17 ± 0.15, 21.49 ± 0.06, 20.84 ± 0.07, 20.86 ± 0.11, 20.48 ± 0.19)	0.50 ± 0.05
DESJ0023–4923 (A)	5.931774	−49.391834	(21.50 ± 0.04, 20.11 ± 0.02, 19.02 ± 0.02, 18.65 ± 0.02, 16.83 ± 0.01)	0.74 ± 0.03
DESJ0023–4923 (1)	5.933479	−49.391714	(22.48 ± 0.08, 21.55 ± 0.05, 20.53 ± 0.05, 20.47 ± 0.07, 17.91 ± 0.02)	0.75 ± 0.04
DESJ0023–4923 (2)	5.9327	−49.3903	…	…
DESJ0025–4133 (A)	6.4894	−41.553807	(21.20 ± 0.07, 19.45 ± 0.01, 18.64 ± 0.01, 18.24 ± 0.02, 18.07 ± 0.04)	0.57 ± 0.05
DESJ0025–4133 (1)	6.491265	−41.555826	(22.71 ± 0.17, 21.50 ± 0.06, 20.84 ± 0.07, 20.44 ± 0.10, 20.39 ± 0.25)	0.44 ± 0.07
DESJ0025–4133 (2)	6.490591	−41.555939	(22.53 ± 0.18, 21.21 ± 0.07, 20.93 ± 0.09, 20.65 ± 0.15, 20.14 ± 0.30)	0.42 ± 0.08
DESJ0030–5213 (A)	7.510464	−52.223393	(21.01 ± 0.03, 19.21 ± 0.01, 18.46 ± 0.01, 18.07 ± 0.01, 17.86 ± 0.02)	0.54 ± 0.05
DESJ0030–5213 (1)	7.509599	−52.224238	(21.82 ± 0.06, 20.80 ± 0.03, 20.26 ± 0.04, 19.91 ± 0.06, 19.50 ± 0.09)	0.74 ± 0.06
DESJ0031–4403 (A)	7.770345	−44.05004	(21.85 ± 0.04, 20.11 ± 0.02, 19.27 ± 0.02, 18.86 ± 0.02, 18.69 ± 0.03)	0.58 ± 0.02
DESJ0031–4403 (1)	7.7707	−44.0491	…	…
DESJ0033–5445 (A)	8.352292	−54.760035	(21.85 ± 0.03, 20.85 ± 0.02, 20.61 ± 0.03, 20.34 ± 0.04, 20.09 ± 0.09)	0.39 ± 0.10
DESJ0033–5445 (1)	8.350841	−54.758944	(21.44 ± 0.02, 20.95 ± 0.02, 20.58 ± 0.03, 20.51 ± 0.05, 20.82 ± 0.22)	0.16 ± 0.06
DESJ0033–5445 (2)	8.350579	−54.76009	(21.99 ± 0.04, 21.59 ± 0.04, 21.41 ± 0.08, 21.49 ± 0.14, 21.28 ± 0.36)	0.16 ± 0.11
DESJ0035–5130 (A)	8.843005	−51.505451	(20.39 ± 0.02, 18.66 ± 0.01, 18.11 ± 0.01, 17.74 ± 0.01, 17.56 ± 0.02)	0.35 ± 0.04
DESJ0035–5130 (B)	8.845253	−51.50674	(21.84 ± 0.03, 20.07 ± 0.01, 19.51 ± 0.02, 19.16 ± 0.01, 18.95 ± 0.03)	0.33 ± 0.03
DESJ0035–5130 (1)	8.845842	−51.506618	(21.73 ± 0.05, 20.83 ± 0.05, 20.29 ± 0.08, 20.01 ± 0.06, 19.34 ± 0.08)	0.81 ± 0.08
DESJ0035–5130 (2)	8.844036	−51.509864	(23.21 ± 0.08, 22.70 ± 0.09, 22.05 ± 0.14, 22.01 ± 0.15, 21.93 ± 0.32)	0.81 ± 0.08
DESJ0035–5130 (3)	8.844082	−51.503093	(22.32 ± 0.05, 21.71 ± 0.05, 21.65 ± 0.13, 21.40 ± 0.10, 20.89 ± 0.18)	0.31 ± 0.12
DESJ0037–4131 (A)	9.362849	−41.530497	(22.52 ± 0.07, 21.04 ± 0.02, 20.00 ± 0.02, 19.54 ± 0.02, 19.28 ± 0.06)	0.69 ± 0.03
DESJ0037–4131 (1)	9.361859	−41.530538	(22.80 ± 0.06, 21.89 ± 0.04, 21.33 ± 0.04, 20.98 ± 0.05, 21.08 ± 0.22)	0.43 ± 0.06
DESJ0037–4131 (2)	9.36239	−41.530983	(22.71 ± 0.06, 21.80 ± 0.04, 21.31 ± 0.04, 20.95 ± 0.05, 20.61 ± 0.14)	0.53 ± 0.06
DESJ0037–4131 (3)	9.363215	−41.531121	(23.09 ± 0.08, 22.16 ± 0.05, 21.79 ± 0.06, 21.53 ± 0.08, 21.36 ± 0.25)	0.45 ± 0.06

Note. System name refers to the arc or lensed source image as shown in Table 2 and in Figures 6–16. Object label refers to lenses (letters) and sources (numbers) within the respective cutouts. All positions (R.A., decl. in J2000), magnitudes and photometric redshifts are drawn from the DESDM database, if available there. The redshift uncertainties have been multiplied by 1.5 times the original estimate, according to the results of Sánchez et al. (2014) for estimating uncertainties calculated using DES photometric redshift measurement codes. *Y*-band photometry is provided where available: supernova fields were only observed in the *Y*-band for those fields that overlap with the wide-field survey. Each system is separated by a horizontal line.

(This table is available in its entirety in machine-readable form.)

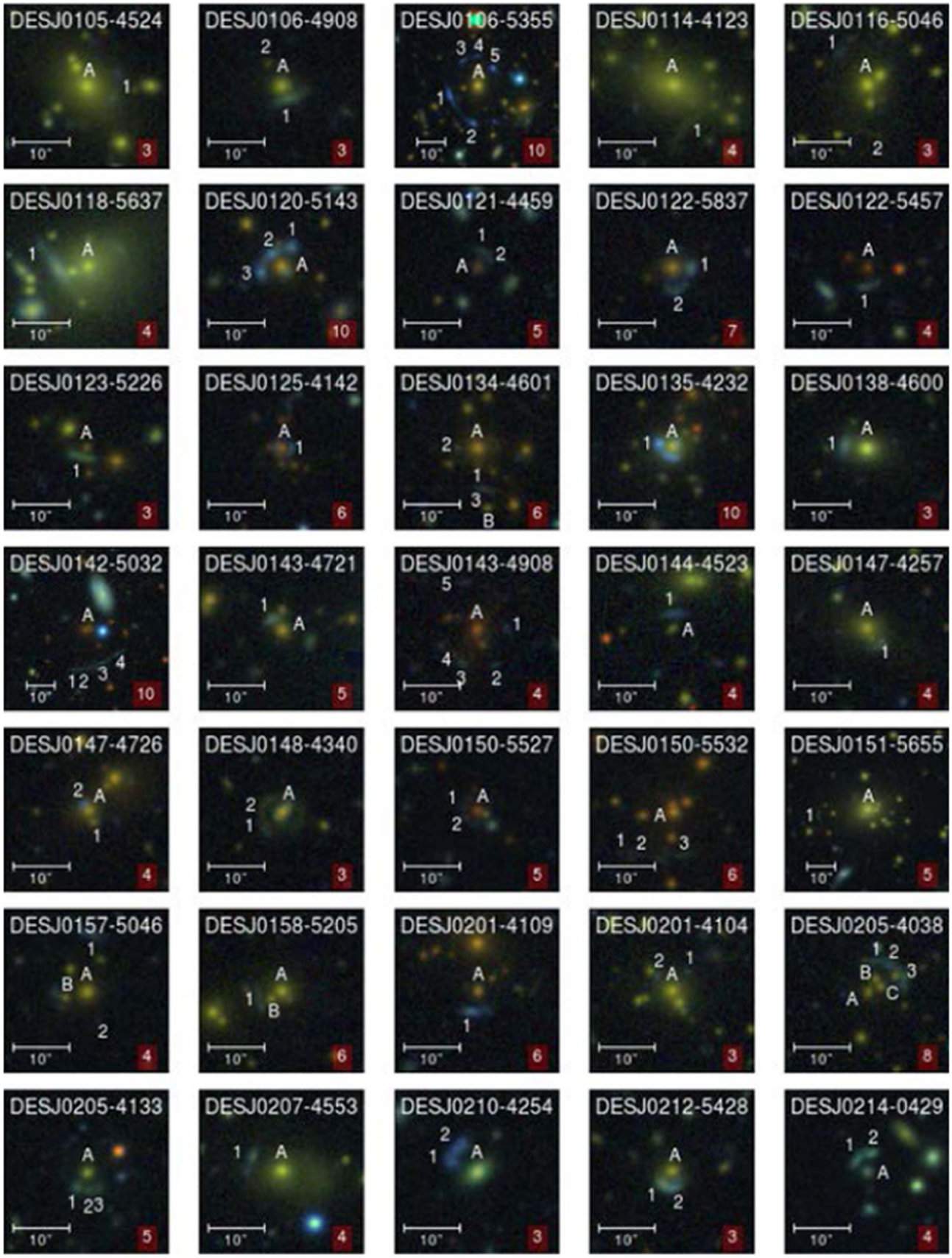

Figure 7. Second page of SL systems with ranks of 3 or more. Each cutout image has the visual inspection ranking displayed in a red box in the lower right hand corner. All images are oriented with north up and east left. Most of the cutouts are $30'' \times 30''$ in size. Some of the largest systems are displayed with $60'' \times 60''$ images, so that they fit well within the cutout. A scale bar $10''$ long is displayed in the lower left hand corner.

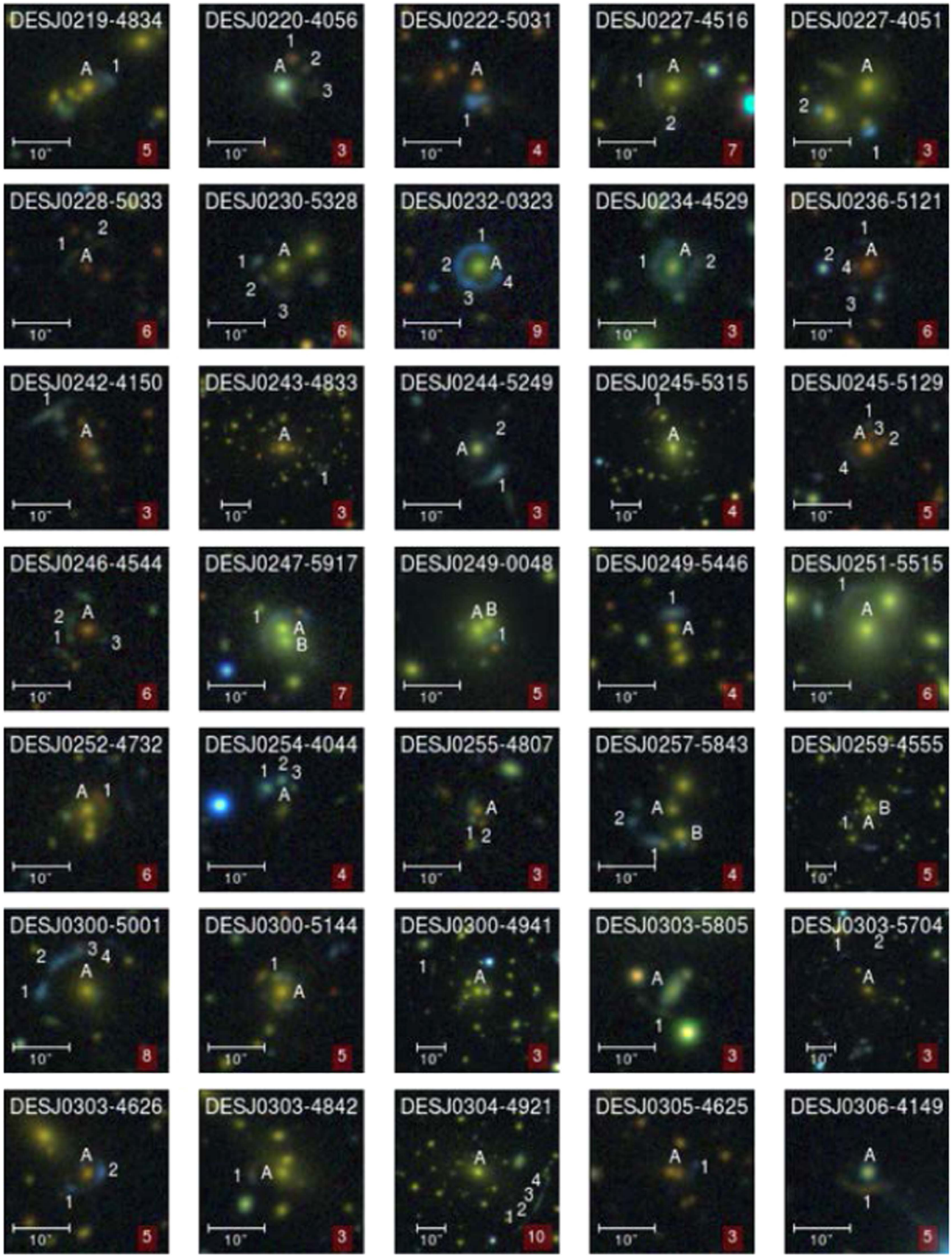

Figure 8. Third page of SL systems with ranks of 3 or more. Each cutout image has the visual inspection ranking displayed in a red box in the lower right hand corner. All images are oriented with north up and east left. Most of the cutouts are $30'' \times 30''$ in size. Some of the largest systems are displayed with $60'' \times 60''$ images, so that they fit well within the cutout. A scale bar $10''$ long is displayed in the lower left hand corner.

Figure 9. Fourth page of SL systems with ranks of 3 or more. Each cutout image has the visual inspection ranking displayed in a red box in the lower right hand corner. All images are oriented with north up and east left. Most of the cutouts are $30'' \times 30''$ in size. Some of the largest systems are displayed with $60'' \times 60''$ images, so that they fit well within the cutout. A scale bar $10''$ long is displayed in the lower left hand corner.

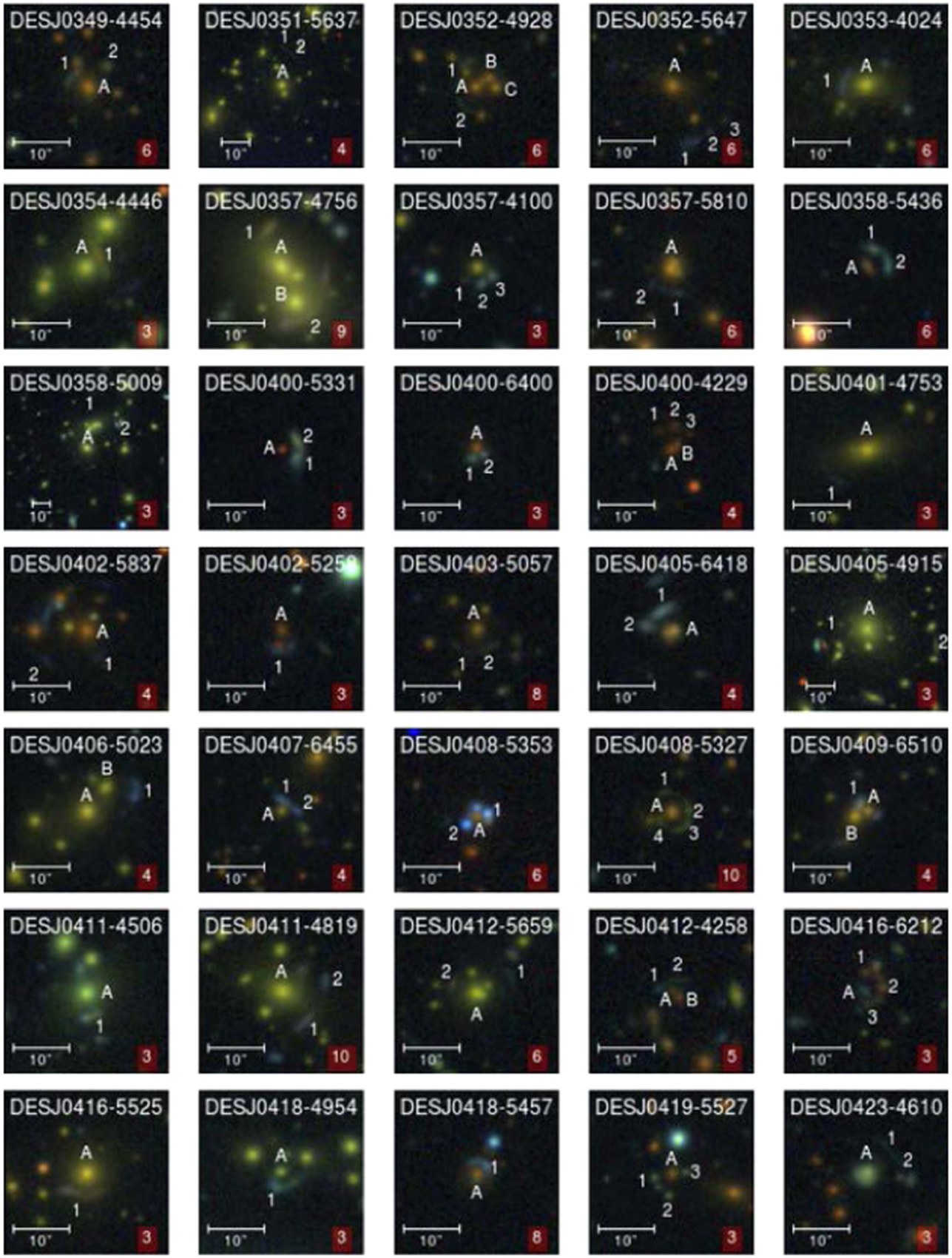

Figure 10. Fifth page of SL systems with ranks of 3 or more. Each cutout image has the visual inspection ranking displayed in a red box in the lower right hand corner. All images are oriented with north up and east left. Most of the cutouts are $30'' \times 30''$ in size. Some of the largest systems are displayed with $60'' \times 60''$ images, so that they fit well within the cutout. A scale bar $10''$ long is displayed in the lower left hand corner.

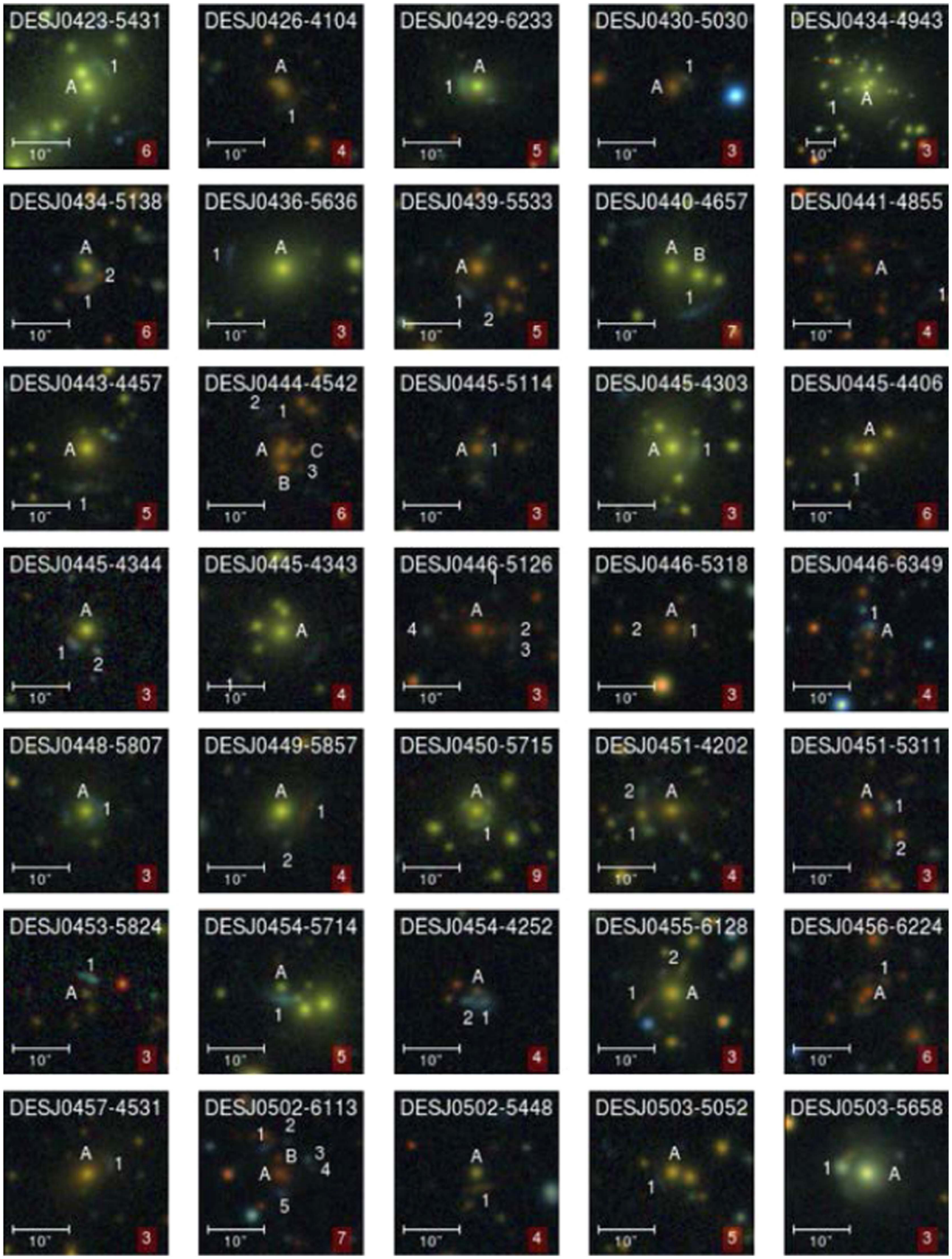

Figure 11. Sixth page of SL systems with ranks of 3 or more. Each cutout image has the visual inspection ranking displayed in a red box in the lower right hand corner. All images are oriented with north up and east left. Most of the cutouts are $30'' \times 30''$ in size. Some of the largest systems are displayed with $60'' \times 60''$ images, so that they fit well within the cutout. A scale bar $10''$ long is displayed in the lower left hand corner.

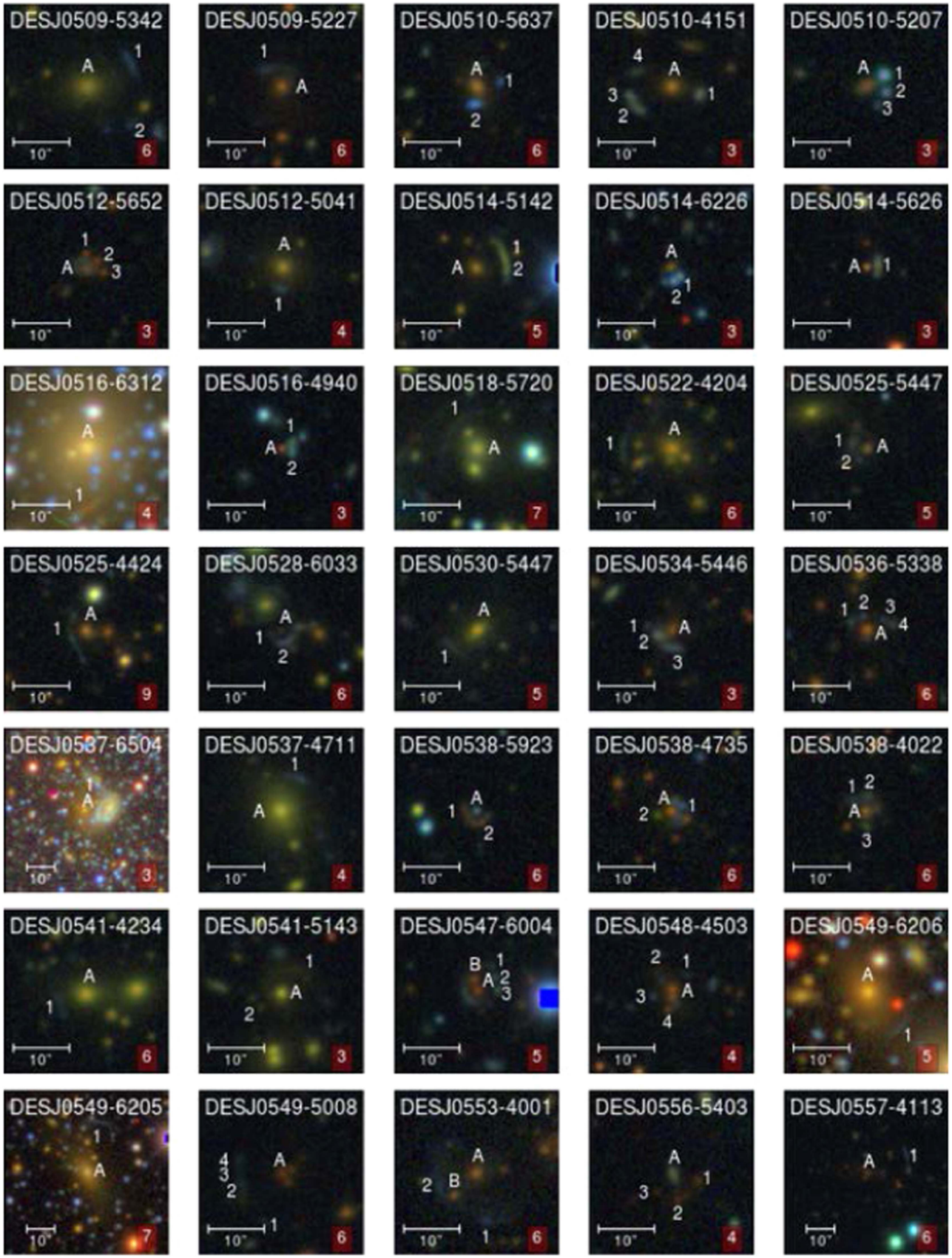

Figure 12. Seventh page of SL systems with ranks of 3 or more. Each cutout image has the visual inspection ranking displayed in a red box in the lower right hand corner. All images are oriented with north up and east left. Most of the cutouts are $30'' \times 30''$ in size. Some of the largest systems are displayed with $60'' \times 60''$ images, so that they fit well within the cutout. A scale bar $10''$ long is displayed in the lower left hand corner.

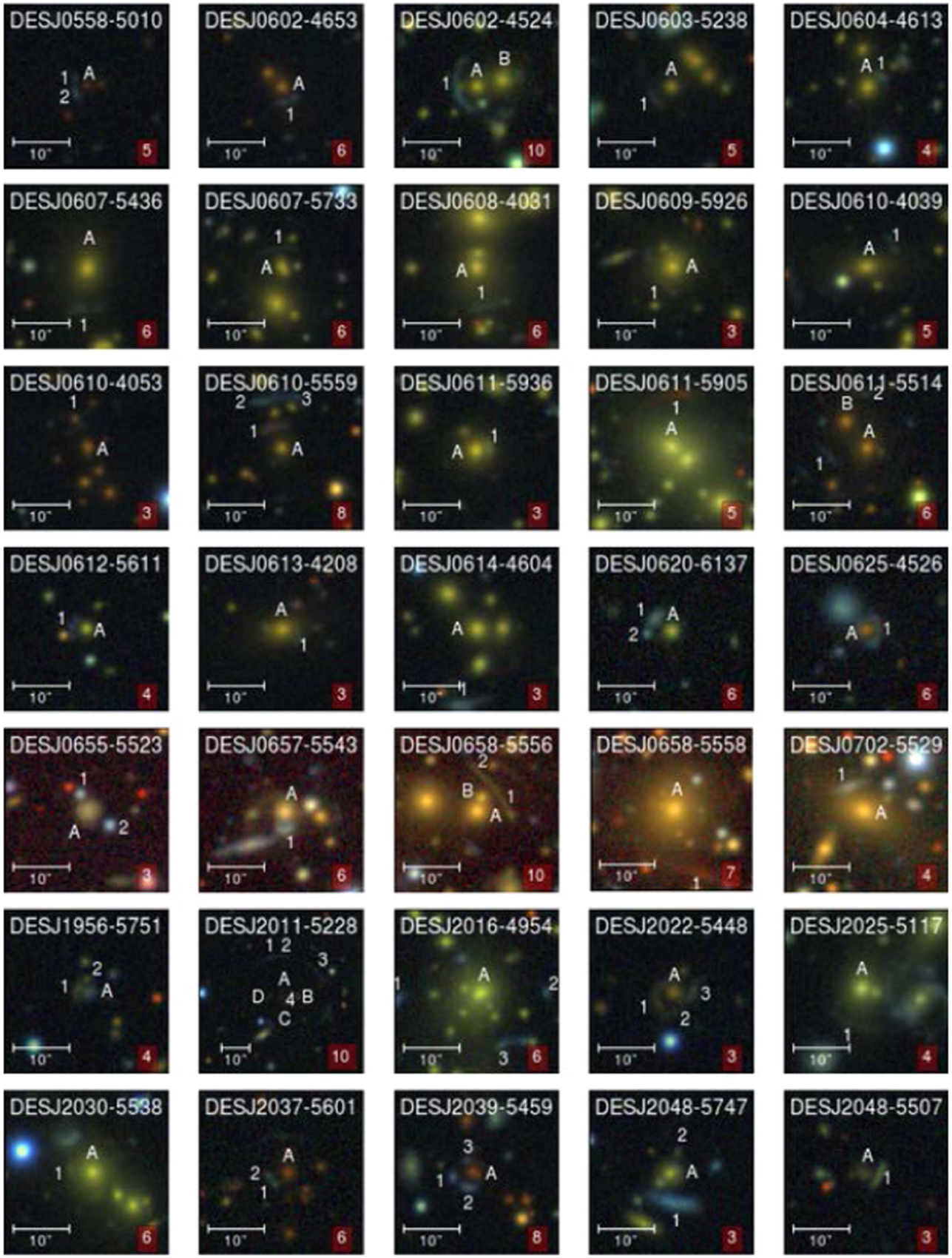

Figure 13. Eighth page of SL systems with ranks of 3 or more. Each cutout image has the visual inspection ranking displayed in a red box in the lower right hand corner. All images are oriented with north up and east left. Most of the cutouts are $30'' \times 30''$ in size. Some of the largest systems are displayed with $60'' \times 60''$ images, so that they fit well within the cutout. A scale bar $10''$ long is displayed in the lower left hand corner.

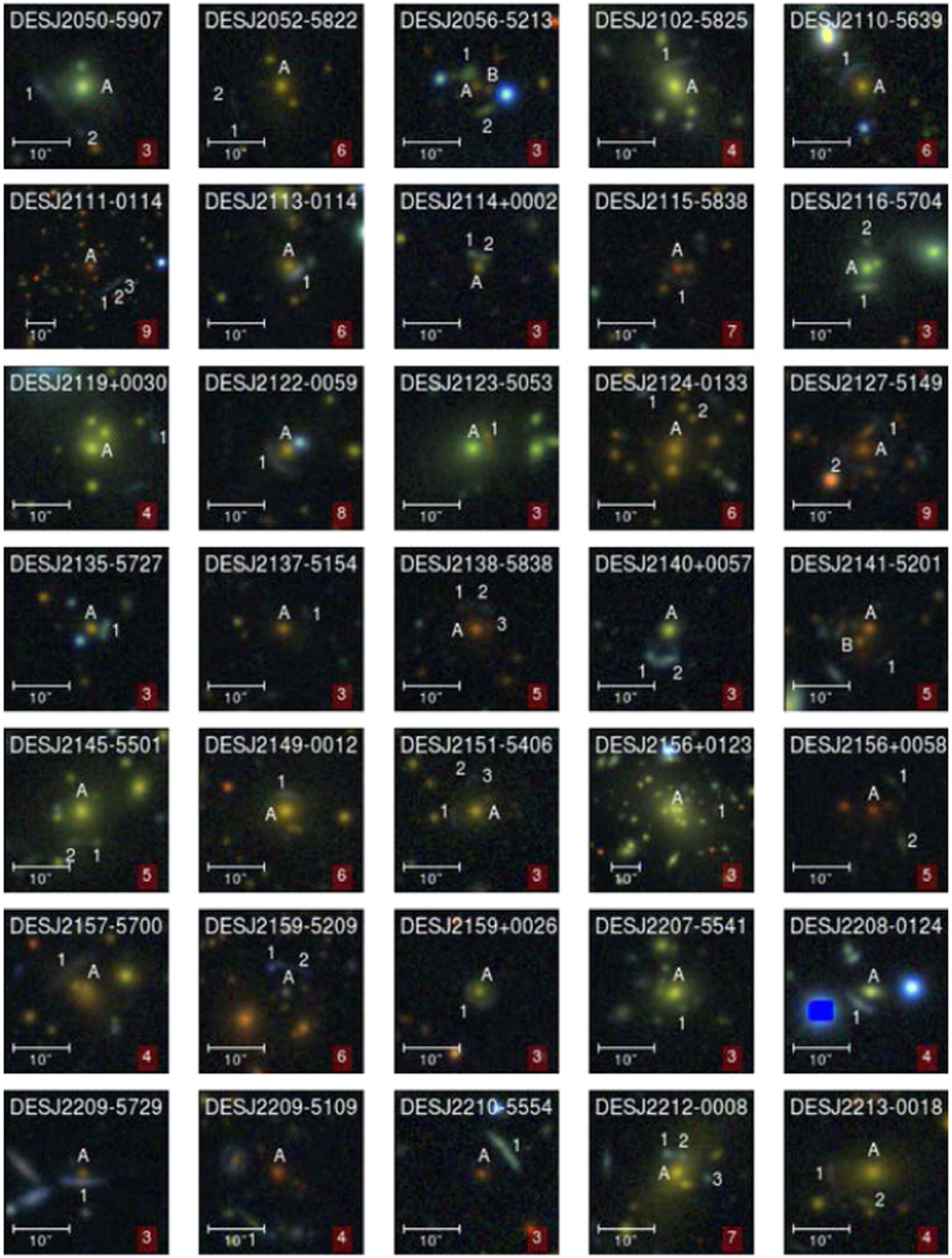

Figure 14. Ninth page of SL systems with ranks of 3 or more. Each cutout image has the visual inspection ranking displayed in a red box in the lower right hand corner. All images are oriented with north up and east left. Most of the cutouts are $30'' \times 30''$ in size. Some of the largest systems are displayed with $60'' \times 60''$ images, so that they fit well within the cutout. A scale bar $10''$ long is displayed in the lower left hand corner.

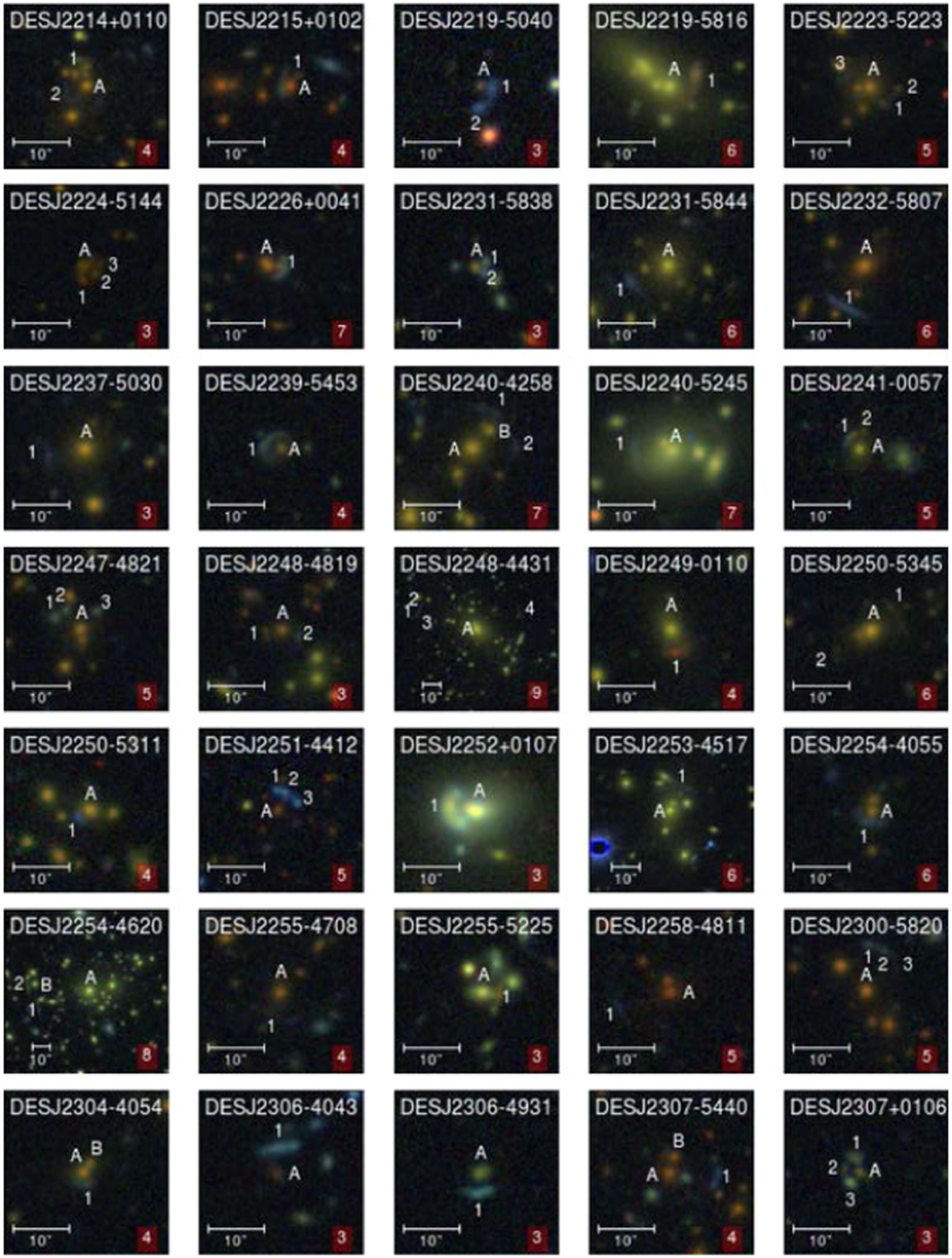

Figure 15. Tenth page of SL systems with ranks of 3 or more. Each cutout image has the visual inspection ranking displayed in a red box in the lower right hand corner. All images are oriented with north up and east left. Most of the cutouts are $30'' \times 30''$ in size. Some of the largest systems are displayed with $60'' \times 60''$ images, so that they fit well within the cutout. A scale bar $10''$ long is displayed in the lower left hand corner.

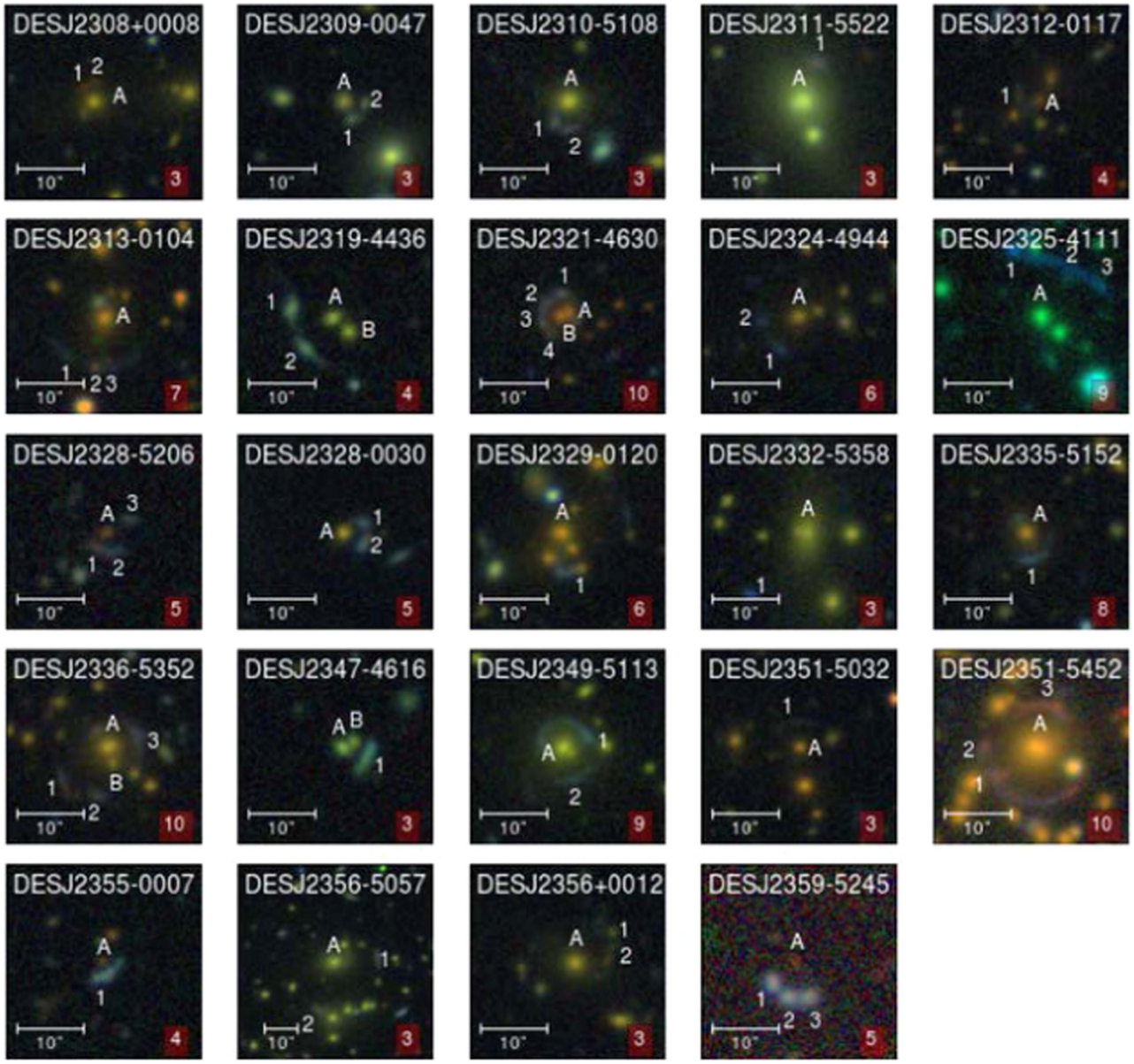

Figure 16. Eleventh page of SL systems with ranks of 3 or more. Each cutout image has the visual inspection ranking displayed in a red box in the lower right hand corner. All images are oriented with north up and east left. Most of the cutouts are $30'' \times 30''$ in size. Some of the largest systems are displayed with $60'' \times 60''$ images, so that they fit well within the cutout. A scale bar $10''$ long is displayed in the lower left hand corner.

bluer source galaxies have weaker spectral break features that will lead to larger photo-z errors, as well as possible catastrophic mistakes. Thus, the source photo-z distribution shown in Figure 17 may not be reliable. In particular, we see that the source photo-z distribution noticeably lies below the lens photo-z distribution at the lowest redshifts. While part of this may result from foreground objects contaminating our candidate source sample, it may also be due to catastrophic photo-z errors scattering true higher-redshift ($z \gtrsim 1$) blue source galaxies to erroneously low photo-z values.

For each system, we measure an average radius of the source images, with respect to the primary lens. The uncertainty on the mean is drawn from the standard deviation on the mean, summed in quadrature with the pixel scale of DES, $0\farcs263$. The pixel scale represents the resolution of DES images, which we use as a minimum uncertainty. The average radius of source images is an approximation for the Einstein radius, and is identical to that when the true source position is directly behind the lens. The image separation distribution is sensitive to a number of inputs such as the halo mass, the lens mass distribution, and the source redshift. It therefore contains information about the cosmological parameters and various scaling relations between galaxy properties and halo mass and can be measured from galaxy to cluster scales (Oguri 2006; More et al. 2016). Figure 18 is the distribution of the radii.

In Section 3.1 we noted that the SPT Collaboration had identified (Bleem et al. 2015) 48 strong lens systems in the SPT data. We found 18 of those in the searches described here. DES did not observe in the locations of 14 of the SPT SL systems during SV or Y1. We do see evidence of strong lensing at the location of 3 of the SPT lenses that we did not identify as strong lensing systems in our searches. The sources, which appear very faint, did not pass the magnitude selection criteria, so we did not scan cutouts for those positions. For the 13

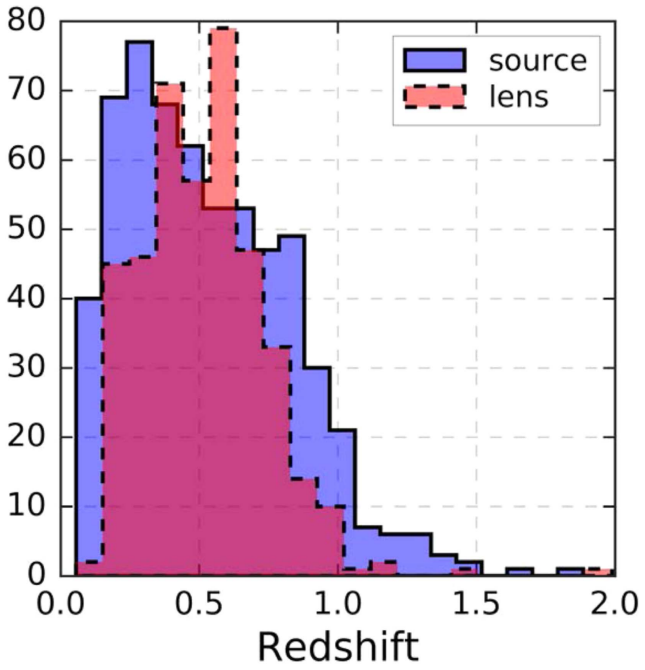

Figure 17. DESDM-calculated photometric redshifts for the sources and lenses. As explained in Section 4, the redshifts of the sources are subject to larger uncertainties.

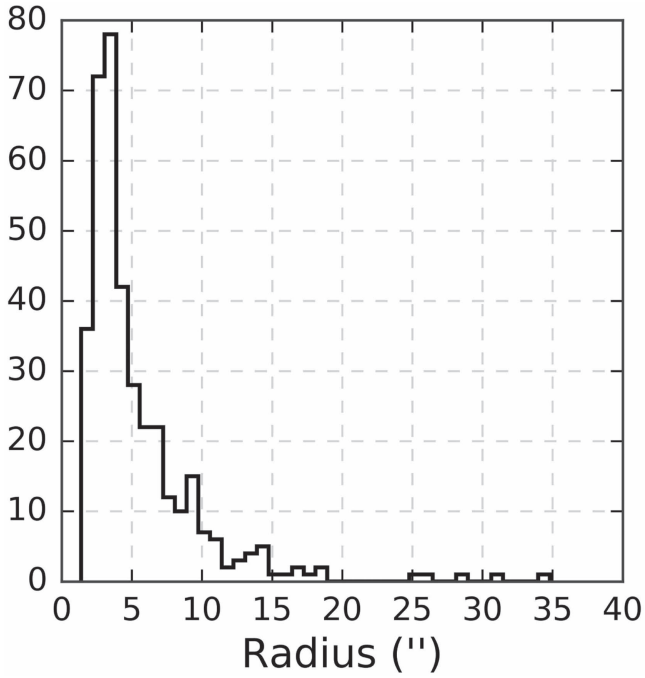

Figure 18. The binned distribution of radii for the lens candidates.

remaining SPT lenses, the DES images do not show any evidence of lensing. The sources are presumably too faint to be identified in the DES coadded data.

We cannot quantify the purity of our strong lens candidate sample because of the presently limited statistics of the follow-up results in B. Nord et al. (2017, in preparation), except to note that a few low-ranked systems (3 or 4), as well as a few higher-ranked systems, are already confirmed and that the higher-ranked systems are expected to have a higher purity than systems with lower rank.

4.1. Notable Systems

We do not remark further on the most obvious candidate lensing systems in our sample, except to ask the reader to peruse the cutout images starting with Figure 6, noting the rankings given in the red box in the lower right corner of each cutout. There are some systems with giant arcs and others with simple configurations, including counter-images. A few of the systems have also been previously reported (and sometimes already confirmed) by DES or other authors, and the appropriate references are given in Table 2. However, we would like to highlight some of our systems for other reasons.

Strong lens systems with red-colored sources are scarce. A number of those systems that we report have sources that have a manifestly red color. These are generally redder than the "red" requirement of the RNA search. Nice examples are DESJ0252-4736, DESJ0434–5138, DESJ0538–5923, DESJ 0658–5558, DESJ2219–5816, and DESJ2351–5452, among others.

Two group-scale systems have both blue and red sources at different radii. DESJ0342–5355 has a red-colored source with radius $4\farcs76$, located on the opposite side of the putative lens from the blue-colored source with radius $10\farcs9$. DESJ0610–5559 has a red-colored source with radius $4\farcs0$, located on the same side of the putative lens as the blue-colored source that has a radius of $9\farcs3$.

5. Summary and Conclusion

We report the results of several searches of the DES SV and Y1 imaging data for strong gravitational lens systems. These searches cover roughly 2000 sq.-deg. and used a combination of techniques. We searched the positions of known SPT and DES galaxy clusters, and we searched the DES catalogs for spatial matches of potential lens and source candidates. For all of the searches we produced a short list of candidates and then evaluated cutouts to identify the most promising systems based on color and morphology. A total of 388,017 cutouts were evaluated. We then assigned those a rank that quantifies our confidence, on those bases, that the system is a potential strong gravitational lens. We provide the R.A. and decl., the magnitudes and photometric properties of the lens and source objects, and the distance (radius) of the source(s) from the lens center for each system. Of the 374 that we found, 350 are presented for the first time. Some of these are striking systems with giant arcs. Some have red-colored sources. Two have both blue and red candidate sources at differing distance from the candidate lens. Using a Gemini Large and Long Program[45] over two years we have spectroscopically confirmed 13 of the systems presented here (Nord et al. 2016; B. Nord et al. 2017, in preparation; Collett et al. 2017; Lin et al. 2017), which is 3.5% of the sample. It is clear that the abundance of candidates means that within DES we are only able to follow-up a small number of the systems. Eventually, we expect most of these will be studied in more detail.

This large catalog of strong lens candidates, presented from a single search effort using uniform data, provides hundreds of ranked strong lensing candidate systems. We expect the variety of configurations will make it useful and valuable as a training

[45] http://www.gemini.edu/node/12599

set for future crowdsourced searches and future automated searches. This catalog also underscores the need for and importance of crowdsourced or automated lens modeling techniques (Birrer et al. 2015; Küng et al. 2015) being developed.[46]

We have recently completed re-processing of the DES data from the first three observing seasons. This will add about 3000 additional sq.-degs. to be searched. We have therefore decided to release this catalogs of strong lens candidates from the DES SV and Y1 catalogs.

We are grateful for the extraordinary contributions of our CTIO colleagues and the DECam Construction, Commissioning and Science Verification teams in achieving the excellent instrument and telescope conditions that have made this work possible. The success of this project also relied critically on the expertise and dedication of the DES Data Management group.

Funding for the DES Projects has been provided by the U.S. Department of Energy, the U.S. National Science Foundation, the Ministry of Science and Education of Spain, the Science and Technology Facilities Council of the United Kingdom, the Higher Education Funding Council for England, the National Center for Supercomputing Applications at the University of Illinois at Urbana-Champaign, the Kavli Institute of Cosmological Physics at the University of Chicago, the Center for Cosmology and Astro-Particle Physics at The Ohio State University, the Mitchell Institute for Fundamental Physics and Astronomy at Texas A&M University, Financiadora de Estudos e Projetos, Fundação Carlos Chagas Filho de Amparo à Pesquisa do Estado do Rio de Janeiro, Conselho Nacional de Desenvolvimento Científico e Tecnológico and the Ministério da Ciência, Tecnologia e Inovação, the Deutsche Forschungsgemeinschaft and the Collaborating Institutions in the Dark Energy Survey.

The Collaborating Institutions are Argonne National Laboratory, the University of California at Santa Cruz, the University of Cambridge, Centro de Investigaciones Energéticas, Medioambientales y Tecnológicas-Madrid, the University of Chicago, University College London, the DES-Brazil Consortium, the University of Edinburgh, the Eidgenössische Technische Hochschule (ETH) Zürich, Fermi National Accelerator Laboratory, the University of Illinois at Urbana-Champaign, the Institut de Ciències de l'Espai (IEEC/CSIC), the Institut de Física d'Altes Energies, Lawrence Berkeley National Laboratory, the Ludwig-Maximilians Universität München and the associated Excellence Cluster Universe, the University of Michigan, the National Optical Astronomy Observatory, the University of Nottingham, The Ohio State University, the University of Pennsylvania, the University of Portsmouth, SLAC National Accelerator Laboratory, Stanford University, the University of Sussex, Texas A&M University, and the OzDES Membership Consortium.

The DES data management system is supported by the National Science Foundation under grant No. AST-1138766. The DES participants from Spanish institutions are partially supported by MINECO under grants AYA2012-39559, ESP2013-48274, FPA2013-47986, and Centro de Excelencia Severo Ochoa SEV-2012-0234. Research leading to these results has received funding from the European Research Council under the European Unions Seventh Framework Programme (FP7/2007-2013), including ERC grant agreements 240672, 291329, and 306478.

We are also grateful to Phillips Academy students Aiden Driscoll, Charles Stacey, Ashley Scott, and Sabine Nix for their contributions to the scanning effort.

[46] https://github.com/DES-SL/EasyLens and http://linan7788626.github.io/pages/Hoopla/index.html

ORCID iDs

C. Furlanetto https://orcid.org/0000-0001-6838-431X
J. Annis https://orcid.org/0000-0002-0609-3987
A. Carnero Rosell https://orcid.org/0000-0003-3044-5150
A. Drlica-Wagner https://orcid.org/0000-0001-8251-933X
J. L. Marshall https://orcid.org/0000-0003-0710-9474
P. Nugent https://orcid.org/0000-0002-3389-0586
G. Tarle https://orcid.org/0000-0003-1704-0781

References

Agnello, A., Treu, T., Ostrovski, F., et al. 2015, MNRAS, 454, 1260
Alard, C. 2006, arXiv:astro-ph/0606757
Allam, S. S., Tucker, D. L., Lin, H., et al. 2007, ApJL, 662, L51
Annis, J., Soares-Santos, M., Strauss, M. A., et al. 2014, ApJ, 794, 120
Aravena, M., Murphy, E. J., Aguirre, J. E., et al. 2013, MNRAS, 433, 498
Bayliss, M. B., Hennawi, J. F., Gladders, M. D., et al. 2011, ApJS, 193, 8
Bayliss, M. B., Rigby, J. R., Sharon, K., et al. 2014, ApJ, 790, 144
Belokurov, V., Evans, N. W., Hewett, P. C., et al. 2009, MNRAS, 392, 104
Bertin, E. 2006, in ASP Conf. Ser. 351, Astronomical Data Analysis Software and Systems XV, ed. C. Gabriel et al. (San Francisco, CA: ASP), 112
Bertin, E. 2011, in ASP Conf. 442, Astronomical Data Analysis Software and Systems XI, ed. D. A. Bohlender, D. Durand, & T. H. Handley (San Francisco, CA: ASP), 435
Bertin, E., & Arnouts, S. 1996, A&AS, 117, 393B
Bertin, E., Mellier, Y., Radovich, M., et al. 2002, in ASP Conf. Ser. 281, Astronomical Data Analysis Software and Systems XI, ed. D. A. Bohlender, D. Durand, & T. H. Handley (San Francisco, CA: ASP), 228
Bettinelli, M., Simioni, M., Aparicio, A., et al. 2016, MNRAS, 461, L67
Birrer, S., Amara, A., & Refregier, A. 2015, ApJ, 813, 102
Birrer, S., Amara, A., & Refregier, A. 2016, JCAP, 08, 020
Blandford, R. D., & Narayan, R. 1992, ARA&A, 30, 311
Bleem, L. E., Stadler, B., de Haan, T., et al. 2015, ApJS, 216, 27
Bonvin, V., Courbin, F., Suyu, S. H., et al. 2017, MNRAS, 465, 4914
Buckley-Geer, E. J., Lin, H., Drbek, E. R., et al. 2011, ApJ, 742, 48
Carlstrom, J. E., Ade, P. A. R., Aird, K. A., et al. 2011, PASP, 123, 568
Collett, T. E. 2015, ApJ, 811, 20
Collett, T. E., & Auger, M. W. 2014, MNRAS, 443, 969
Collett, T. E., Auger, M. W., Belokurov, V., et al. 2012, MNRAS, 424, 2864
Collett, T. E., Buckley-Geer, E., Lin, H., et al. 2017, arXiv:1703.08410
de Bom, C. R., Makler, M., Albuquerque, M. P., et al. 2017, A&A, 597, A135
Diehl, H. T., Abbott, T. M. C., Annis, J., et al. 2014, Proc. SPIE, 9149, 91490V
Diehl, H. T., Allam, S. S., Annis, J., et al. 2009, ApJ, 707, 686
Drlica-Wagner, A., Sevilla-Noarbe, I., Rykoff, E. S., et al. 2017, ApJ, in press (arXiv:1708.01531)
Faure, C., Kneib, J.-P., Covone, G., et al. 2008, ApJS, 176, 19
Flaugher, B., Diehl, H. T., Honscheid, K., et al. 2015, AJ, 150, 150
Gavazzi, R., Marshall, P. J., Treu, T., et al. 2014, ApJ, 785, 144
Gavazzi, R., et al. 2008, ApJ, 677, 1046
Gómez, P. L., Valkonen, L. E., Romer, A. K., et al. 2012, AJ, 144, 79
Greve, T. R., Viera, J. D., Weiss, A., et al. 2012, ApJ, 756, 101
Hennawi, J. F., et al. 2008, AJ, 135, 664
Joseph, R., Courbin, F., Metcalf, R. B., et al. 2014, A&A, 566, A63
Jullo, E., et al. 2010, Sci, 329, 924
Kessler, R., Marriner, J., Childress, M., et al. 2015, AJ, 150, 172
Koopmans, L. V. E., Bolton, A., Treu, T., et al. 2009, ApJL, 703, L51
Kostrzewa-Rutkowska, Z., Wyrzykowski, Ł., Auger, M. W., et al. 2014, MNRAS, 441, 3238
Kubik, D. 2007, M.S. thesis, Northern Illinois Univ.
Kubo, J. M., Allam, S. S., Annis, J., et al. 2009, ApJ, 696, 61
Kubo, J. M., Allam, S. S., Drabek, E., et al. 2010, ApJL, 724, L137
Kubo, J. M., & Dell'Antonio, I. P. 2008, MNRAS, 385, 918
Küng, R., Saha, P., More, A., et al. 2015, MNRAS, 447, 2170
Lanusse, F., Ma, Q., & Li, N. 2017, arXiv:1703.02642
Li, N., Gladders, M. D., Rangel, E. M., et al. 2016, ApJ, 828, 54
Lin, H., Buckley-Geer, E., Agnello, A., et al. 2017, ApJL, 838, L15

Lin, H., Buckley-Geer, E., Allam, S. A., et al. 2009, ApJ, 699, 1242
Link, R., & Pierce, M. J. 1998, ApJ, 502, 63
Marshall, P. J., Verma, A., More, A., et al. 2016, MNRAS, 455, 1171
Mehlert, D., Seitz, S., Saglia, R. P., et al. 2001, A&A, 379, 96
Menanteau, F., González, J., Juin, J.-B., et al. 2010a, ApJ, 723, 1523
Menanteau, F., Hughes, J. P., Barrientos, L. F., et al. 2010b, ApJS, 191, 349
Menanteau, F., Hughes, J. P., Sifón, C., et al. 2012, ApJ, 748, 7
Meneghetti, M., Bartelmann, M., Dahle, H., & Limousin, M. 2013, SSRv, 177, 31
Mohr, J. J., Armstrong, R., Bertin, E., et al. 2012, Proc. SPIE, 8451, 84510D
More, A., Cabanac, R., More, S., et al. 2012, ApJ, 749, 38
More, A., Verma, A., Marshall, P. J., et al. 2016, MNRAS, 455, 1191
Newman, A. B., Ellis, R. S., & Treu, T. 2015, ApJ, 814, 26
Nord, B., Buckley-Geer, E., Lin, H., et al. 2016, ApJ, 827, 51
Oguri, M. 2006, MNRAS, 367, 1241
Oguri, M., & Marshall, P. J. 2010, MNRAS, 405, 2579
Ostrovski, F., McMahon, R. G., Connolly, A. J., et al. 2017, MNRAS, 465, 4325
Oyaizu, H., et al. 2008a, ApJ, 674, 768
Oyaizu, H., et al. 2008b, ApJ, 689, 709
Paraficz, D., Courbin, F., Tramacere, A., et al. 2016, A&A, 592, A75
Petrillo, C. E., Tortora, C., Chatterjee, S., et al. 2017, arXiv:1702.07675
Pettini, M., Christensen, L., D'Odorico, S., et al. 2010, MNRAS, 402, 2335
Reed, S. L., McMahon, R. G., Banerji, M., et al. 2015, MNRAS, 454, 3952
Refsdal, S. 1964, MNRAS, 128, 307
Reichardt, C. L., Stalder, B., Bleem, L. E., et al. 2013, ApJ, 753, 127
Rozo, E., Rykoff, E. S., Abate, A., et al. 2016, MNRAS, 461, 1431
Rozo, E., Rykoff, E. S., Koester, B. P., et al. 2009, ApJ, 703, 601
Rykoff, E. S., Rozo, E., Busha, M. T., et al. 2014, ApJ, 785, 33
Rykoff, E. S., Rozo, E., Hollowood, D., et al. 2016, ApJS, 224, 1
Sánchez, C., et al. 2014, MNRAS, 445, 1482
Schechter, P. L., Bailyn, C. D., Barr, R., et al. 1997, ApJL, 475, L85
Seidel, G., & Bartelmann, M. 2007, A&A, 472, 341
Song, J., Zenteno, A., Stalder, B., et al. 2012, ApJ, 761, 22
Sonnenfeld, A., Chan, J. H. H., Shu, Y., et al. 2017, PASJ, submitted (arXiv:1704.01585)
Staniszewski, Z., Ade, P. A. R., Aird, K. A., et al. 2009, ApJ, 701, 32
Stark, D. P., Auger, M., Belokurov, V., et al. 2013, MNRAS, 436, 1040
Sunyaev, R. A., & Zel'dovich, Y. B. 1972, CoASP, 4, 173
Suyu, S. H., Auger, M. W., Hilbert, S., et al. 2013, ApJ, 766, 70
Suyu, S. H., Bonvin, V., Courbin, F., et al. 2017, MNRAS, 468, 2590
The Dark Energy Survey Collaboration 2016, MNRAS, 460, 1270
Treu, T., & Ellis, R. S. 2014, ConPh, 56, 17
Wen, Z.-L., Han, J.-L., & Jiang, Y.-Y. 2011, RAA, 11, 1185
Wiesner, M. P., Lin, H., Allam, S. S., et al. 2012, ApJ, 761, 1
Wittman, D. M., DellÁntonio, I. P., & Hughes, J. P. 2006, ApJ, 643, 128
Xu, B., Postman, M., Meneghetti, M., et al. 2016, ApJ, 817, 85
Zhang, Y., McKay, T. A., Bertin, E., et al. 2014, PASP, 127, 1183
Zitrin, A., Menanteau, F., Hughes, J. P., et al. 2013, ApJL, 770, L15